Variability in the Geostrophic Flow of the Agulhas Current, an Investigation of Sea Surface Height Obtained from Altimetry Data

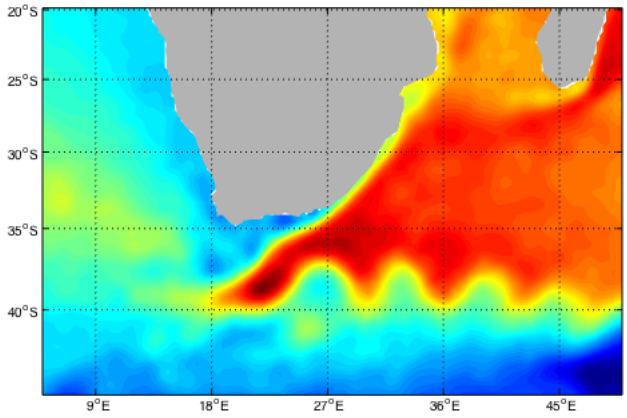

Karen Fosse Sivertsen

June 2015

MASTER'S THESIS

Geophysical Institute

University of Bergen

Preface

This thesis is written as a part of the Master's Programme in Meteorology and Oceanography with specialization in Physical Oceanography at University of Bergen. The work was carried out during the academic year 2014/2015. The master thesis is part of the SCAMPI project (Seasonal to decadal Changes Affecting Marine Productivity: an Interdisciplinary investigation, project No.: 234205 / H30) funded by the Research Council of Norway and build on bilateral research collaborations between the Marine Research Institute and the Nansen-Tutu Centre at University of Cape Town, the Nansen Environmental and Remote Sensing Center in Bergen, and the University of Bergen.

Bergen, 15 June 2015

Karen Fosse Sivertsen

Acknowledgment

I would like to thank the following persons for their great help during this last year.

I would like to thank my supervisors Professor Johnny A. Johannessen at Nansen Environmental and Remote Sensing Center/University of Bergen and Dr. Bjorn Backeberg at University of Cape Town/Nansen-Tutu Center for giving me the opportunity to take part of the SCAMPI project and maintain my relation to the oceanographic research community at UCT: Johnny, for sharing his knowledge and constructive feedback; and Bjorn, for running the model and giving me the courtesy to work with the data, and for making my stay in Cape Town very productive.

I would also like to thank Dr. Roshin Raj at Nansen Environmental and Remote Sensing Center for introducing me to the Aviso-world of data in the initial phase.

And to those little helpers along the way: Tor Gammelsrød, for encouraging words and for pointing me towards the right people; Marjoline Krug, for discussions and ideas about my topic; Knut Barthel, for finding a way with my MatLab routines; and Raymond Sellevold, for all those technical quick fixes and unwinding lunch breaks.

And last but no least: my parents. Thanks to the kindest person I know, for putting his own work aside and pulling me through the last phase; dad, you're my hero! Mom, thanks for giving me that hug when I needed it the most.

K.F.S.

Abstract

The distinct and robust structure of the greater Agulhas Current regime southeast of southern Africa was depicted in the spatial pattern of the absolute dynamic topography. As a part of Work Package 3: Environmental driver, indicators, interactions and variability, and under Key Question 7: What are the physical drivers of annual cycles and seasonal events affecting marine ecosystems in the oceans of southern Africa?, this thesis investigated the variability of the Agulhas Current system through altimetry data from Aviso and model simulation data from HYCOM. The seasonal absolute dynamic topography anomalies are slightly higher and the seasonal geostrophic velocities are slightly stronger in the austral summer and fall compared to the winter and spring seasons. In the Agulhas Return Current the along-track altimetry data (track 96) showed clear interannual variability. Spectral analysis indicated that the dominating variability have periods of 1.8 and 4.3 years. In comparison, no interannual variability was detected for the Agulhas Current, except for the occasional negative anomalies indicating the passages of meanders, known as Natal Pulses. The Agulhas Current simulated by HYCOM corresponded well to that observed by the gridded altimetry data. The mean position of the Agulhas Return Current, however, was about two degrees too far south and lacked the characteristic meanders that were well displayed by the gridded altimetry data. Moreover, also the mean position of the Agulhas Retroflection simulated by HYCOM differed from that observed by the altimetry data. The position of the Agulhas Retroflection represented by HYCOM data varied more than 18 degrees in east-west direction, with its westernmost position at $5^{\circ}E$. In contrast, the gridded altimetry data depicted an east-west variation of about seven degrees, with its westernmost position at $14^{\circ}E$.No reliable indicator of the retroflection position was found, most likely due to the high non-linear and complex dynamics that are present in this region.

Contents

Chapter 1

Motivation and Objectives

1.1 Background

This thesis is a part of the SCAMPI project which primary aim is to identify and analyse patterns of seasonal to decadal variability in southern African marine environments, ecosystems and living resources, to assess medium- to long-term changes that have occurred in these patterns and to investigate and predict the likely consequences of such change for food security and biodiversity (SCAMPI, 2014). On the east coast of southern Africa the ecosystems are impacted by the frequent presence of mesoscale eddies, Natal pulses and dynamic upwelling generated by the Agulhas Current (AC). The AC is a western boundary current, and with its high horizontal gradients both in sea surface temperature as well as in sea surface height it has become an attractive region for remote sensing case studies (Lutjeharms, 2006a).

Lutjeharms (2006a) stated that a detailed description of the geoid will allow absolute surface topography of the ocean, and not just the anomalies, to be derived from satellite altimetry. This will make it possible to describe temporal changes to all components of the greater Agulhas Current system. The altimetry data used in this study are related to the latest, and assumed most accurate, GOCE-based geoid. The time series of altimetry data is now more then 20 years long, and temporal variability and changes almost up to decadal timescales can be studied.

Literature Survey

Numerical ocean models show annual variations in the Agulhas Current (AC) transport, with a minimum in austral winter (August) and a maximum in austral summer (February) (Lutjeharms, 2006a).

Matano et al. (2002) link the seasonal changes of the transport of the AC to the large-scale circulation in the tropical Indian Ocean. Model simulations show that the AC transport has a seasonal variation with a maximum at the transition between the austral winter and the austral spring and a minimum between the austral summer and the austral autumn. Evidence are presented that the seasonal cycle of the western Indian Ocean is the result of the oscillation of barotropic modes forced directly by the wind.

Matano et al. (1999) use a model with a northern boundary at 20°S to show that the seasonal variability in the AC is dominated by local wind forcing. Biastoch et al. (1999) use a model that extends to 6.5°S to allow for contributions from the Mozambique Channel to be taken into account. This model exhibits seasonality in AC transport with the contribution from the Mozambique Channel, at 23°S, varying from near zero in February/March to over 20 Sv in August. At 32°S, the southward transport of the AC is weakest in January and March and the October/November maximum is displaced from the Mozambique Channel maximum in August. This lag suggests an advective link between the seasonal signal in the Mozambique Channel and that off the South African coast.

Model runs by van Sebille et al. (2009) show that a smaller (larger) AC transport leads to larger (smaller) Indian-Atlantic inter-ocean exchange. When transport is low, the AC detaches farther downstream from the African continental slope. Moreover, the lower inertia suppresses generation of anti-cyclonic vorticity. These two effects cause the Agulhas Retroflection (AR) to move westward and enhance leakage. A decrease in the Agulhas leakage is compensated by an increase in the Agulhas Return Current (ARC) transport.

Observational studies by e.g. Bryden et al. (2005) and Matano et al. (2008) were unable to highlight evidence of a seasonal cycle in the AC.

Matano et al. (1998) present evidence for the existence of seasonal variability in sea surface height (SSH) anomaly in the AR region. Three years of TOPEX/Poseidon altimeter data are used to estimate seasonal changes in the mesoscale SSH variability. There is a seasonal oscillation in

SSH variability characterized by a maximum during the austral summer and a minimum during austral winter. The seasonal differences in variability are the result of displacements of the mean path of the AC, plausibly explained by weaker transport of the AC during winter, and stronger during summer, in combination with topography and local winds.

Krug and Tournadre (2012) use 18 years of SSH observations from altimeters and 7 years of high frequency sea surface temperature imagery to study the variability of the AC transport. They show that the geostrophic current speed at the current's core exhibits distinct seasonal variations, with stronger flow observed in austral summer. The annual cycle is the dominant mode of variability of the absolute geostrophic currents speed. An annual cycle in the AC core geostrophic flow is in agreement with results from numerical ocean models (e.g. Matano et al., 2002) and seems to confirm the link between the wind-driven variability in the source regions of the AC and its transport further downstream.

Transport of Indian Ocean waters into the South Atlantic via the Agulhas leakage has increased during the past decades in response to the change in wind forcing (Biastoch et al., 2009). This contributes to the observed salinification of South Atlantic thermocline waters. Model studies show that the amount of Agulhas leakage is linked to the latitudinal shifts in the southern hemisphere westerlies.

What remains to be done?

Although many studies have indicated some kind of seasonality within the greater Agulhas Current system, they have not coincided significantly to establish a predictable pattern of annual variability. Local wind stress is proposed as a forcing mechanism for most of the detected seasonality.

For variability patterns of interannual to decadal timescales, few studies have been made. The time series of altimetry data is now long enough to investigate variability almost up to decadal timescales. Additionally, the more accurate geoid will provide more detailed results.

Improved knowledge of the variability patterns in the geostrophic flow of the AC could help provide an explanation for variability in marine ecosystems of southern Africa, and thus contribute to the SCAMPI project. Also the AC's role in the salinity-heat budget of the AMOC will be better estimated with knowledge of any variability pattern.

1.2 Objectives

The topic of this thesis is Variability in the geostrophic flow of the Agulhas Current, an investigation of sea surface height obtained from altimetry data, and falls under Key Question 7: What are the physical drivers of annual cycles and seasonal events affecting marine ecosystems in the oceans of southern Africa?, of Work Package 3: Environmental drivers, indicators, interactions and variability, of the (SCAMPI, 2014) project.

The main objectives of this Master's project are

1. to investigate seasonal and interannual variability patterns in the dynamic topography and geostrophic flow of the Agulhas Current.

2. to compare altimetry data and HYCOM data.

3. to discuss possible drivers and impacts of the variability patterns discovered.

1.3 Structure of the thesis

The thesis is organized as follows. Chapter 2 gives an introduction to the theory and equations that forms the basis of the project. Chapter 3 gives insight to the data and the approach used. The results are presented through figures in chapter 4 and further discussed in chapter 5. Chapter 6 sums up the conclusion of the thesis, and provides a brief outlook.

Chapter 2

Background: Theory

2.1 The Agulhas Current, a Western Boundary Current

The following presentation of the Agulhas Current (AC) is based on a thorough description by Lutjeharms (2006a).

The AC is the western limb of the wind-driven, anti-cyclonic circulation of the South Indian Ocean. The AC has some unusual characteristics that distinguish it from other western boundary currents. Western boundary currents are narrow and intense poleward flows driven by the zonally integrated wind-stress curl of the adjacent basins. The AC system has all these main characteristics that define it as a western boundary current, except that the extent of zonal integration across the South Indian Ocean for its driving force is unclear. The subtropical ocean gyre here is not a simple ocean-wide movement, but is concentrated to the west and interrupted by the landmass of Madagascar. The most unique feature of the AC is tied to the limited poleward extend of the African continent, and the opportunity this presents for a transfer of warm AC water into the South Atlantic Ocean.

The main source for the AC is through recirculation in the wind driven sub-gyre. Also the flow through the Mozambique Channel (MC) and the East Madagascar Current (EMC) has been conceived as tributary to the AC. Volume transport estimates are retrieved from Hermes et al. (2007), and are not inconsistent with previous estimates. The flow in the MC is dominated by a train of anti-cyclonic eddies that increase in size as they move poleward. The annual mean transport through the channel is $8.4 Sv$ ($1 Sv = 10^6 m^3 s^{-1}$). The EMC has shown to be a miniature

western boundary current, and the southern termination of this current is a source of considerable mesoscale turbulence where eddies are formed before they travel south-westwards. In a section east of Madagascar the EMC transport is estimated to $16 Sv$ flowing southward, increasing to $35 Sv$ flowing westward in a section south of Madagascar. The increase in volume flux is due to the amount of recirculation included in the calculations. The volume flux of the AC increases downstream, with a maximum flow of $62 Sv$ at $35° S$. As the source flow is interrupted by the presence of Madagascar, the AC may possibly be under the influence of a seasonally varying surface flow in that part of the Equatorial and Indian Ocean that is under the influence of the Monsoon regime.

The AC system can be divided into four branches; the northern AC, the southern AC, the Agulhas Retroflection (AR), and the Agulhas Return Current (ARC). The northern AC is said to begin at $27° S$, between Maputo and Durban (see figure 2.1), and there is no continuum between the flow in the MC and the AC as earlier projected. The flow path of this upstream component is along a narrow shelf with a steep shelf slope, which leads to a characteristically stable flow that shows little variation in the current trajectory. The mean speed and energy is exceptionally high and show little variability, including seasonal variability. The existence of a compensating undercurrent has been established for this northern branch of the AC.

In contrast to this stability, the northern AC also experiences large, solitary meanders. These meanders origin in the Natal Bight, just north of Durban, and are known as Natal Pulses. Intense, mid-ocean eddies has been thought to be the origin in the triggering of these pulses, combined with the relaxed steepness of the continental shelf and the characteristic dynamics of the region. This meandering feature is unique to this particular western boundary current.

Along its path the AC grows downstream in both size and strength. At the latitude of Port Elizabeth (see figure 2.1) the continental shelf starts to become much wider, forming the broad Agulhas Bank south of Africa. The behavior of the current also starts to change dramatically here with large lateral meanders forming part of the current trajectory downstream from this point. This is the southern branch of the AC. The shelf is bathymetrically divided at about $21° E$ with a long, wider shelf with a low shoreward gradient to the east and a narrower, more steeply sloped shelf to the west. The shallowest central part forms a division between these two sides and an effective partition for their water masses. The southern AC detaches itself from the shelf edge

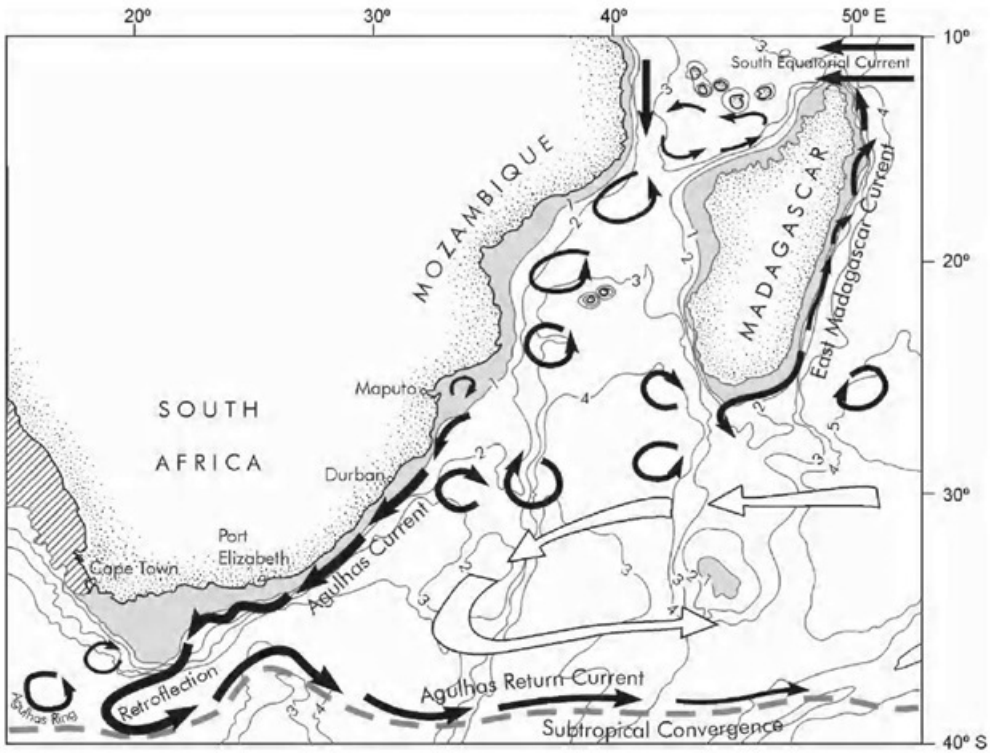

Figure 2.1: Sketch of the greater Agulhas Current system and its source regions. Adapted from (Lutjeharms, 2006b).

somewhere around 21°E, depending on its instantaneous volume flux.

The limited poleward extent of the African continent allows for a direct inter-ocean exchange of subtropical water masses. In the AR the AC turns back on itself in a tight loop (see figure 2.1), and most of the water flows back into the South Indian Ocean through the ARC (see figure 2.1). Occasionally, the high mesoscale variability in the AR region leads to spawning of Agulhas Rings (see figure 2.1), leaking warm, salty water into the South Atlantic Ocean. The AR, ring shedding and Natal Pulses have all been discovered or verified and established as oceanographic facts through satellite remote sensing. The effect of spawned rings has been a focus of observational and modeling investigations. The behavior of the rings once they have been spawned has been monitored and described, giving the result that each ring behaves different from the next. The timing of spawning events is also considered to be triggered by the Natal Pulse. According to Biastoch et al. (2009) the leakage is also influencing the salinity transport and the overturning circulation in the North Atlantic.

2.2 Altimetry

Numerous studies have provided solid evidence for the reliability of altimetric products to accurately depict ocean motion (e.g. Capet et al. (2014) and Mazloff et al. (2014)). The AC system is a region with large mesoscale variability, with eddies, meanders, rings, filaments, waves and fronts, which all play a role in transporting mass, heat, salt and nutrient. High space and time resolution is needed to resolve this variability. Satellite altimetry has made a unique contribution in observing and understanding mesoscale variability (Traon and Dibarboure, 2004).

2.2.1 Principles of altimetry

Satellite altimeters are nadir-looking (straight down), cloud cover independent, radars with active microwave sensors. The altimeter emits regular pulses and records the return signal after reflection from the Earth's surface. The travel time, the magnitude and shape of each return signal are recorded. The orbit repeat cycle, the time it takes before the satellite flies over the exact same spot, can vary between 3 and 35 days. The longer the revisit interval the finer the spatial sampling grid (Robinson, 2004).

The essential altimetric measurement is the distance between the satellite and the mean sea surface, R_{alt}, known as the range (see figure 2.2). The height of the satellite, H_{sat}, is measured relative to a reference level. The reference level is a regular ellipsoid-shaped surface with frame of reference fixed on the rotating Earth (approximately the shape of the Earth at sea level). The height, h, of the sea above the reference level is given by

$$h = H_{sat} - R_{alt} \tag{2.1}$$

The accuracy and precision of h, therefore depends on both H_{sat} and R_{alt}, and varies with time and place (Robinson, 2004).

A pulse of microwave radiation is emitted in the direction of the sea surface, and the time, t, it takes for it to return is measured. The speed of light, c, is used to calculate the distance, R_{alt}. Some corrections are performed to ensure that the shortest distance is measured, and to determine the size of the footprint. The microwave frequency must lie in the range $2-18GHz$ (S-, C-, X- or K_u-band) as the sea is a good reflector in these bands, and the leading edge of

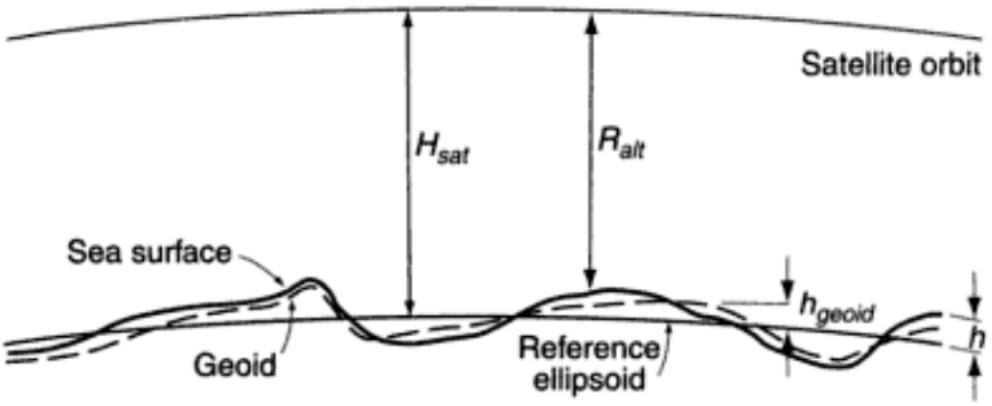

Figure 2.2: Sketch showing the satellite orbit relative to the sea surface, the geoid and the reference ellipsoid. Adapted from (Robinson, 2004).

the pulse should be sharply defined (Robinson, 2004). For a resolution of x the required pulse length is less than $\frac{x}{c}$.

On a flat ocean surface the point closest to the sensor is encountered at $t = \frac{R_{alt}}{c}$. Because the pulse expands as a spherical shell, the footprint of the pulse is a circle whose area grows linearly with time. At time $t = \frac{R_{alt}}{c} + \tau$ the circle evolves into a ring with varying width but constant area coverage. The first reflected signal arrives back at the altimeter at time $t = 2\frac{R_{alt}}{c}$ and its power grows linearly from zero until at time $t = 2\frac{R_{alt}}{c} + \tau$. Now, when the illuminated area becomes constant, the power of the return signal levels out. As the ring increases in diameter, the radar incidence becomes increasingly off-nadir, and the specular reflected energy gradually reduces (Robinson, 2004).

The precision of R_{alt} depends on the time sampling frequency of the returning signal. Elapsed time is measured from the centre of the emitted pulse until the time when the rising edge of the return pulse reaches half the maximum. The pulse length determines the size of the illuminated circle as the reflected energy reaches its maximum (Robinson, 2004).

The sea is not perfectly flat and is often very rough, so the shape of the leading edge of the return pulse is dependent on the wave height. The first reflection of energy is from the topmost crest of the waves, earlier than for the flat surface, but the reflected energy reaches maximum when the trailing edge reaches the lowest trough. The reflected signal received at the sensor is drawn out over time. However, the time from the mid-point of the pulse emission to the mid-point of the rising edge of the return signal still corresponds to the two-way travel time to the

mean sea surface. Thus the effect of ocean waves is averaged out (Robinson, 2004).

Most altimeters are pulse-limited, meaning that the shape of the return signal is dictated by the length of the pulse. Beam-limiting altimeters require large antennas that have to point precisely towards the nadir. Using a pulse-limited altimeter one avoids the need to constrain the spread of the emitted beam and it automatically samples the nadir point (Robinson, 2004). Each individual return signal is very noisy, but averaging many successive pulses can reduce this.

The distance from the satellite to the sea surface, R_{alt}, must be corrected for processes that slow down the pulse transmission below the speed of light. In the troposphere, gases and liquid water are accounted for by the dry and wet correction, respectively. In the ionosphere the ionospheric correction accounts for dielectric properties (Robinson, 2004). Rain causes problem for the altimeter, as patchy cells of heavy rain cause localized attenuation of the return signal that distort the waveform and produce errors in the tracking algorithm.

The measured range, R_{alt}, tends to be overestimated when microwave radiation reflects the rough sea surface. Ocean waves have shorter sharper peaks and longer flatter troughs, thus the height distribution in ocean waves has a skew distribution with median height lower than the mean height. Assumed that the electromagnetic scattering from the sea surface is symmetrical about the mean height, there is a skewness bias. The higher the sea state the greater the bias, and it is estimated as a linear function of the significant wave height. There is also a bias related to the strength of the electromagnetic scattering, referred to as the electromagnetic bias, which also overestimates the range. The shorter roughness elements have greater amplitude at the crests than at the troughs, and for nadir-viewing radars the backscatter power is greater per unit area from scattering elements in the troughs than in the crests. The potential for error in sea state bias estimation is greatest where sea state is high (Robinson, 2004).

To get the height of the sea surface relative to the Earth, the precise position of the satellite must be known. The orbit depends on the dynamic forces acting on the satellite. Deviations in the orbit from the pure ellipse are variations in the gravitational attraction of the Earth, Moon and Sun, the drag of the atmosphere, and the pressure of direct and Earth-reflected solar radiation. Spatial inhomogeneity of mass distribution over the Earth's surface is reflected in the geoid shape. Local gravity varies temporally with tide-generating potential as mass is redistributed in response to tidal forces. Gravitational variability can cause radial orbit perturbations of up to

10 km from the elliptical form. The higher the altitude the smaller the atmospheric drag and smaller the orbit model errors (Robinson, 2004).

2.2.2 The GOCE geoid as reference level for altimetry

The geoid represents the distribution of gravity over the Earth, at a height h_{geoid} above the reference ellipsoid (see figure 2.3). The geoid is defined as the equipotential surface, at mean sea level, of the effective gravitational field of the Earth. This incorporates Earth-rotation forces and the gravitation of the solid Earth, the ocean itself and the atmosphere. By definition the geoid is normal to the local effective gravity force.

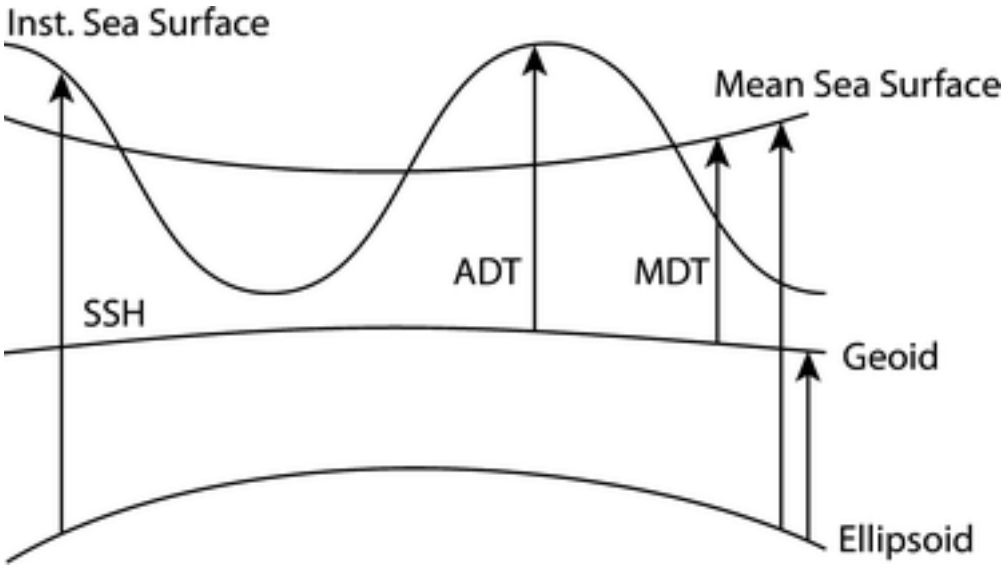

Figure 2.3: Sketch of the connection between Sea Surface Height (SSH), Sea Level Anomalies (SLA), Absolute Dynamic Topography (ADT), Mean Dynamic Topography (MDT), Mean Sea Surface (MSS) the Geoid and the Ellipsoid. Adapted from (Johannessen et al., 2014).

Factors that contribute to h are the tidal height, h_{tide}, the local response of the ocean to the atmospheric pressure distribution, h_{atm}, and displacement of the sea surface associated with the motion of the ocean (ocean dynamic topography), h_{dyn}. This give

$$h = h_{dyn} + h_{geoid} + h_{tide} + h_{atm} \tag{2.2}$$

For ocean dynamics h_{dyn} is of interest, and we rewrite equations 2.1 and 2.2 to get

$$h_{dyn} = H_{sat} - R_{alt} - h_{geoid} - h_{tide} - h_{atm} \tag{2.3}$$

This is the slope relative to the geoid, allowing for tides and atmospheric pressure (Robinson, 2004).

The Gravity Field and Steady-State Ocean Circulation Explorer (GOCE) satellite mission was launched 17 March 2009, with the aim to determine the static component of the Earth's gravity field with a resolution of 1-2 cm for the geoid at a global scale of at least 100 km (Johannessen et al., 2003).The altimetry data used in this thesis are related to the latest GOCE-based geoid. Applying GOCE's geoid to altimetry data amplifies the signal of currents. The geoid is determined in the mean-tide system relative to the Topex-ellipsoid (Rio et al., 2014).

Deviations between the sea surface and a geopotential surface are known as the dynamic topography of the ocean (see figure 2.3). The significant improvement of the GOCE derived gravity field improves the estimated mean dynamic topography (MDT) and the mean ocean circulation (Bosch et al., 2014). The MDT is defined as the difference of the mean sea surface (MSS) height and the static geoid (G) (Johannessen et al., 2003):

$$MDT = MSS - G \tag{2.4}$$

Knowledge of the marine geoid has improved through satellite gravity measurements from the NASA GRACE and ESA GOCE missions. After having subtracted the geoid from the MSS and eliminated the short wavelength geoid signals by filtering, a useful estimate of MDT is obtained. Satellite altimeters have been operating for the last 20 years. The latest release of this data is related to new GOCE-based geoid and MDT. The GOCE-based geoid provides a reliable representation of the MDT and the mean ocean surface circulation (Rio et al., 2014).

2.2.3 Estimation of surface geostrophic velocity from altimetry data

The sea surface dynamical topography allows for estimation of the surface geostrophic current, or the portion of the surface current in geostrophic balance. This surface geostrophic flow is a principal contribution to the large-scale ocean flow. This is particularly true for the intense western boundary currents, where the geostrophic contribution in the upper ocean provides foremost of the total current (Talone et al., 2014).

The mean ocean surface geostrophic velocities are derived from the MDT as horizontal derivatives and can be observed by GOCE down to a spatial resolution of 100 km (Rizos et al., 2014). Isolines of constant MDT are usually considered as a stream function for the large-scale ocean surface circulation, which the surface geostrophic currents are directed along (Johannessen et al., 2014).

Seasonal mean absolute surface geostrophic velocities are estimated by replacing MDT with absolute dynamic topography (ADT) (see figure 2.3). ADT is determined as the sum of MDT and monthly mean sea-level anomaly (SLA) data:

$$ADT = MDT + SLA \tag{2.5}$$

2.2.4 Consecutive altimeter missions

Continuous time series of altimetry measurements, as the ones we have from ERS-1, ERS-2 and Envisat, and TOPEX/Poseidon (T/P), Jason-1 (J-1) and Jason-2 (J-2), enable investigation of long-term sea level change. To assemble a precise climate data record, we must determine the measurement biases inbetween the satellite missions. Data comparisons during the period when two satellites fly over the same track within a minute of each other (210 days for T/P and J-1, and 180 days for J-1 and J-2), work as a calibration/validation period for the instruments and the data, as the satellites should be observing the same real ocean variability. These missions are crucial to reveal and precisely determine biases (Nerem et al., 2010).

To monitor the global change in mean sea level a stable, accurate, and consistent orbit reference over the entire time span is required. Precise orbits based on consistent geophysical modeling strategies and a single reference frame across all missions, along with the adaption

of a consistent ground reprocessing strategy, have enabled the isolation and identification of subtle remaining differences (Beckley et al., 2010).

At least two altimeter missions are required to monitor mesoscale variability. During the tandem missions between T/P and J-1, and J-1 and J-2, the oldest satellite is moved to fly midway between two adjacent original ground tracks. This gives a separation of 1.4° in longitude and doubles the spatial resolution, which has allowed synoptic mapping of large eddies (Traon and Dibarboure, 2004). Mesoscale circulation studies are impossible without the ocean variability correction. To extract the SLA, one removes the mean profile, MSS, from the individual sea surface height (SSH) measurements:

$$SLA = SSH – MSS \tag{2.6}$$

Crossover adjustments remove residual biases by reduction of altimeter noise and removal of long wavelength errors (e.g. orbit error) while preserving most of the mesoscale signal. By further filtering of the SLA data the altimeter noise is reduced and the cross-track velocity is estimated from the sea level gradients (Traon and Dibarboure, 2004).

2.3 Geostrophy from Absolute Dynamic Topography

The geostrophic balance assumes that the Coriolis force balances the horizontal pressure gradient (Gill, 1982). The equations for geostrophic balance are derived from the equations of motion assuming rapidly rotating fluids where the Coriolis acceleration strongly dominates the various acceleration terms. We further consider homogeneous fluids, where the horizontal velocities are much larger than the vertical, $w << u, v$, the only external force is gravity, and frictional effects are ignored. The lowest-order equations governing such fluids are the following simplified equations of motion:

$$-fv = -\frac{1}{\rho_0}\frac{\partial p}{\partial x} \tag{2.7}$$

$$+fu = -\frac{1}{\rho_0}\frac{\partial p}{\partial y} \tag{2.8}$$

$$\frac{\partial u}{\partial x} + \frac{\partial v}{\partial y} + \frac{\partial w}{\partial z} = 0 \tag{2.9}$$

where $f = 2\Omega \sin\phi$ is the Coriolis parameter, ρ_0 is the density and p the pressure.

This reduced set of equations bring us to conclude that the vertical derivative of the horizontal velocity must be identical to zero ($\frac{\partial u}{\partial z} = \frac{\partial v}{\partial z} = 0$). When solving the momentum equations 2.7 and 2.8 in terms of the velocity components we find the corollary that the velocity vector (u, v) is perpendicular to the vector $(\frac{\partial p}{\partial x}, \frac{\partial p}{\partial y})$. This latter vector is the pressure-gradient, and the flow is across gradient, rather than down gradient as it would be in a non-rotating viscous flow, and are navigated along lines of constant pressure, called isobars. This also implies that no pressure work is performed either on the fluid or by the fluid. Hence, once initiated, the flow can persist without a continuous source of energy. Where f is positive (northern hemisphere), the current flows with the high pressure on the right. Where f is negative (southern hemisphere), the current flows with the high pressures on the left. Applied at the surface, the geostrophic approximation leads to the relation that surface geostrophic currents are proportional to the surface slope. A level surface is a surface of constant gravitational potential, and no work is required to move along a frictionless level surface.

For a homogeneous fluid, the dynamic pressure, p, is independent of depth ($\frac{\partial p}{\partial z} = 0$). In the absence of a pressure variation above the fluid surface (e.g., uniform atmospheric pressure over the ocean), this dynamic pressure is

$$p = \rho_0 g h \tag{2.10}$$

Where g is the gravitational acceleration and h is the surface elevation. Substitution into equations 2.7 and 2.8 gives the surface geostrophic current equations:

$$v_s = \frac{g}{f}\frac{\partial h}{\partial x} \tag{2.11}$$

$$u_s = -\frac{g}{f}\frac{\partial h}{\partial y} \tag{2.12}$$

where g is gravity, h is the height of the sea surface above the level surface, and v_s and u_s are the meridional and zonal surface geostrophic velocities, respectively.

The topography of the sea surface, h, is the height of the sea surface relative to a particular level surface, the geoid. Thus, according to equations 2.11 and 2.12, the surface geostrophic currents are proportional to the slope of the topography, a quantity that can be measured by satellite altimeters if the geoid is known. The topography is approximately one hundredth of the geoid undulations. This means that the shape of the sea surface is dominated by local variations of gravity. Substituting h in equations 2.11 and 2.12 with ADT, the absolute dynamic topography from our altimetry data, we can calculate surface geostrophic currents.

$$v_s = \frac{g}{f}\frac{\partial ADT}{\partial x} \tag{2.13}$$

$$u_s = -\frac{g}{f}\frac{\partial ADT}{\partial y} \tag{2.14}$$

Chapter 3

Data and Approach

The data used in this thesis are along-track and gridded products from altimetry, and high-resolution model data from HYCOM. MatLab is used to plot figures for further analysis of the data.

3.1 Altimetry Data

This study is based on more than two decades of continuous altimetry data from TOPEX/Poseidon (T/P), Jason-1 (J-1) and Jason-2 (J-2). T/P was launched in August 1992, J-1 in December 2001 and J-2 in June 2008 (see table 3.1) (Talone et al., 2014). The satellites are first sent into the phase A orbit, which gives the ground track time series used in this study. After the next satellite is launched and the two satellites have flown over the same area for some time, the oldest of the two is redirected to a new orbit, phase B, mid-way between the phase A ground tracks. From the phase A time series we can investigate the global mean sea level change from late 1992 to the present. The altimeter data in this study are the Ssalto/Duacs version 15, released 15th of April 2014. This version has som changes from the previously released data sets (Duacs/AVISO, 2014). The altimeter products were produced by Ssalto/Duacs and distributed by Aviso, with support from Cnes (http://www.aviso.altimetry.fr/duacs/).

The new reference period is 20 years long (1993-2012) as opposed to the previously seven-year (1993-1999) period (Duacs/AVISO, 2014). This means that mean dynamic topography (MDT) and mean sea surface (MSS) values are representative of this new reference period. The change

Table 3.1: Launch date, date for entering the phase B orbit*, and end date listed for the three altimeter missions.

	TOPEX/Poseidon	Jason-1	Jason-2
Launch Date	10/08/1992	07/12/2001	20/06/2008
New Orbit*	15/09/2002	14/02/2009	–
End date	18/01/2006	01/07/2013	still operating

of reference period integrates the evolution of the sea level in terms of trends and interannual signals, which leads to better interannual signals and oceanic anomalies.

New up-to-date standards are applied to the whole altimeter dataset (Duacs/AVISO, 2014), including new solutions for the orbit, tide, and sea state bias, reaper ionospheric solution, and updated solutions for the dry troposphere, and high resolution dynamic atmospheric correction. In addition, the temporal coverage by twin/triplet missions is extended.

The orbit configuration of 9.9156 days is the best compromise for spatial and temporal resolution, and was chosen to measure large-scale ocean variability and avoid aliasing from tidal frequencies. The orbit is prograde and non-sun-synchronous. The high orbit altitude of 1336km is chosen to minimize atmospheric drag and gravity forces, so to make the orbit determination easier and more accurate. The inclination of 66° gives a 90% coverage of the worlds ice-free ocean. Table 3.2 lists technical data for the three missions.

Table 3.2: Technical aspects for the three altimeter missions in phase A orbit.

ALTIMETER	TOPEX/Poseidon	Jason-1	Jason-2
Reference Altitude (Equator)	1336 km	1336 km	1336 km
Inclination	66.039°	66.039°	66.039°
Repeat Cycle	9.9156 days	9.9156 days	9.9156 days
Passes per Cycle	254	254	254
Ground track separation (Equator)	315 km	315 km	315 km
Longitude at Equator of Pass 1	99.9242°	99.9242°	99.9242°
Acute Angle at Equator	39.5°	39.5°	39.5°
Orbital Velocity	7.2 km s^{-1}	7.2 km s^{-1}	7.2 km s^{-1}
Ground Scanning Velocity	5.8 km s^{-1}	5.8 km s^{-1}	5.8 km s^{-1}
Emitted Frequency	13.575 GHz K_u-band	5.3 GHz C-band	($3K_u$-1C-$3K_u$)
Pulse Repetition Frequency	4200 Hz	1200 Hz	2060 Hz
Pulse Duration	102.4 micro sec.	102.4 or 32 micro sec.	–
Bandwidth	320 MHz	320 or 100 MHz	–

3.1.1 Along-track products

The ground tracks for phase A of the T/P, J-1 and J-2 missions over the AC region are shown in figure 3.1. The ground tracks are 315 km apart (at Equator), and together with the repeat cycle of 9.9156 days this give a coverage of the region that are able to capture mesoscale dynamics.

For the along-track data the focus is on track 96 descending just east of Port Elisabeth (yellow line in figure 3.1). The track covers both the AC and the ARC and is believed to display the temporal variations in a representative way. The along-track data comes as near-real time, for operational purposes, and delayed time products, as used in this study. Delayed time products can be either filtered or unfiltered. The unfiltered data series is validated and corrected for long wavelength errors, it keeps the full $1Hz$ resolution, meaning that for a given date, the number of measurements is larger than for the filtered. Filtered data is filtered and subsampled to reduce the uncorrelated measurement noise, in addition to being validated and corrected for long wavelength errors (Duacs/AVISO, 2014).

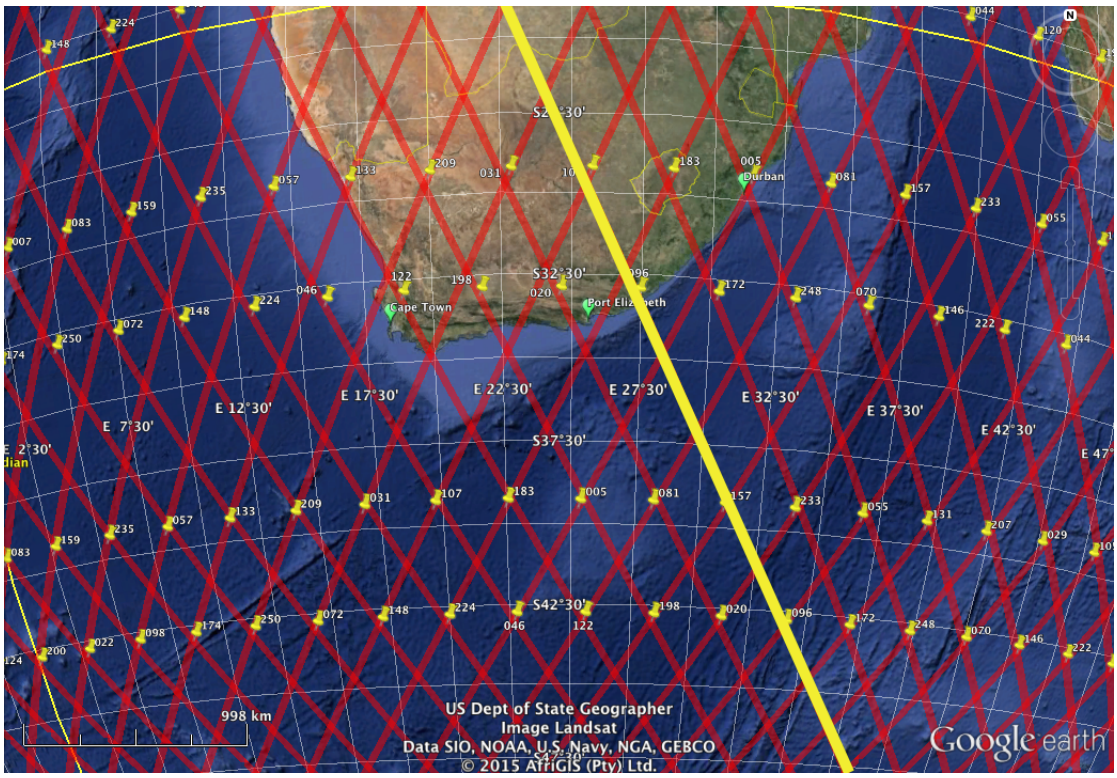

Figure 3.1: Ground track coverage for phase A of TOPEX/Poseidon, Jason-1 and Jason-2. Track 96 is marked with a yellow line. Satellite tracks retrieved from Aviso and overlaid map in Google Earth.

Time series, from September 1992 to May 2014, of unfiltered sea level anomalies (SLA) and absolute dynamic topography (ADT) data along track 96 are used in this analysis. Equation 2.5 states that any temporal variation in ADT comes solely from temporal variations in SLA. Nevertheless, aware that they will provide the same result, Hovmoller plots of both SLA and ADT are plotted to investigate any temporal variability pattern. The cross-track component of the sea surface geostrophic velocity is calculated from the along-track slope in ADT (in accordance to equation 2.14). The distance between two consecutive data points is calculated from latitude and longitude values, yielding $\sim 6.2km$ varying slightly with latitude. Data points farther than one step apart ($\sim 6.2km$) are ignored in the calculations, as they give uncertain values for the slope. Also outlying values of difference in ADT are ignored when calculating the surface geostrophic velocity, as they disturb the mean signal. The temporal resolution of these plots are 9.9156 days.

A spectral analysis of ADT at $39.5°S$, or more accurate $39.4955°S$, is performed to investigate variability in the ARC on interannual timescales. ADT data from the along-track dataset are extracted to create a time series. 17 out of 790 passes for this latitude are missing data. To be able to run a FFT-algorithm and do a spectral analysis for this time series an interpolation of ADT data onto these data points is necessary.

The distance between two consecutive data points along track 96 is $\sim 6.2km$ or 1 second. Setting the limit for interpolation at maximum 3 data points away from $39.5°S$ yields a maximum distance of $\sim 18.6km$ or 3 seconds. 9 out of the 17 points that missed data had available data within this limit both to the north and the south and the mean of the two closest ADT values was calculated to represent the ADT at these points. 5 out of the remaining data points only had available ADT data within this limit on one side, either to the north or south, and this value was interpolated to represent the ADT at these points. For the remaining 3 points no data was available within or close to this limit. To fulfill the requirement of a homogeneous time series, an interpolation of the mean value between the ADT at $39.5°S$ for the passes before and after were used. The time between two passes is 9.9156 days.

3.1.2 Gridded products

A limitation of altimetry data is that it only covers the surface layer of the ocean, but on the other side the coverage is global and steady in time. The delayed time gridded altimetry products are either two-sat merged or all-sat merged. The all-sat merged products are made using all satellite missions available at a given time. Sampling and long wavelength errors determination are improved to better the quality in this product. The two-sat merged products are based on two missions at the most to maintain homogeneity over the time period, though the quality of the data is not the best possible. The gridded altimeter products used in this thesis are delayed time and all-sat merged. In relation to figure 3.1 that shows the ground tracks of only one mission, the all-sat merged gridded products have even better coverage. For the gridded products the main change in the new version of Ssalto/Duacs products is that the spatial resolution is changed from $\frac{1}{3}^\circ \times \frac{1}{3}^\circ$ on the Mercator grid with to the Cartesian $\frac{1}{4}^\circ \times \frac{1}{4}^\circ$. This gives an improved precision and, together with shift in the grid point location from the middle to the bottom left corner of a pixel, gives a better resolution. This resolves phenomenon with an extent down to $50-75km$.

The new Ssalto/Duacs version uses updated parameters for the mapping process (optimal interpolation). This leads to more accurate mapping of the mesoscale by using more accurate correlation scales, taking into account the spatial variability of the signal. New ADT products are computed using the new MDT, which uses the recent geoid mean field and in-situ dataset. The delayed-time gridded files are now produced with a daily temporal resolution, compared to a weekly resolution in the former products.

Both seasonal means and seasonal anomalies of ADT and seasonal mean surface geostrophic velocities are calculated and plotted. The methodology Backeberg et al. (2012) uses for HYCOM data, is adapted to the gridded altimetry data. A trajectory representing the AC core is tracked by calculating a reference value, SSH_{ref}. SSH_{ref} is the mean SSH within $lon \in [30,33]$, $lat \in [-32.5,-28]$ and $depth \in [500,3000]$. The contour of the value is traced along its path from the Mozambique Channel to the ARC east of 45°. The maximum westward position of the contour defines the position of the retroflection and is saved for further investigation. Monthly climatological contours of SSH_{ref}, as well as monthly positions of the retroflection position are plotted.

3.2 HYCOM

The Hybrid Coordinate Ocean Model (HYCOM) is a primitive equation model that smoothly inter-changes the vertical coordinates between z-level coordinates for resolving upper-ocean mixed layer processes, isopycnic in the stratified open ocean, and sigma-coordiantes that follow the bathymetry in the shallow coastal regions (Bleck, 2002). To simulate the greater AC region HYCOM involves two models. A basin scale model of the Indian and Southern Ocean (INDIA) with a horizontal resolution ranging from 30 to 40 km, and a nested, regional model for the AC system (AGULHAS) with a horizontal resolution of 9 to 11 km, adequate to resolve the mesoscale dynamics as the Rossby radius of deformation is about 30 km in this region (Backeberg et al., 2008). The basin-scale model INDIA provides boundary conditions for the regional model of the AC. The vertical discretization in both models uses 30 hybrid layers. Neither of the models include tides. The AGULHAS model is initialized from the equilibrium field of INDIA, interpolated to the high-resolution grid. Atmospheric forcing fields for both models were provided at six hourly intervals. Additional forcing fields include cloud cover, precipitation, exchange of heat and momentum at the surface, and river runoff (as negative salinity flux).

HYCOM combines the optimal features of isopycnic-coordinate and fixed-grid ocean circulation models within one framework (Bleck, 2002). The model conveniently resolves regions of vertical density gradients such as the thermocline and surface fronts. HYCOM provides a reasonable representation of the mean circulation features in the region. The stable AC, in addition to the mesoscale variability, associated with eddies and meanders are in good agreement with the observations (Backeberg et al., 2014). Limitations include too high levels of sea surface height (SSH) variability, trajectories of eddies are to regular and consistent, and the ARC and its variability is too far to the south resulting in a positive SSH bias. The position and mesoscale variability of the AR are sensitive to the representation of the stratification of intermediate water masses used in the simulation (Backeberg et al., 2015).

The free run model simulations (courtesy of Dr. Bjorn Backeberg, NTC/UCT) gave weekly values of SSH for 30 model years (1980-2009). Every model year has twelve model months, which again consist of four model weeks. To track the AC a reference value, SSH_{ref}, is calculated in the same manner as explained for the gridded altimetry data in order to obtain time series of

the position of the retroflection. The output from HYCOM is analysed in comparison with the gridded altimeter products, with a special emphasis on the position of the AR.

Chapter 4

Results

4.1 Gridded Maps

The spatial pattern of the mean value of the absolute dynamic topography (ADT) (figure 4.1) exhibits the distinct structure of the greater Agulhas Current system. Monthly ADT data from the gridded altimetry product from Aviso are averaged for the period 1993-2013. The spatial patter of the mean ADT clearly reveals the northern boundary of the Agulhas Current (AC), the position of the Agulhas Retroflection (AR), and the southern boundary of the meandering Agulhas Return Current (ARC).

The seasonal mean of the ADT is shown for the four austral seasons; summer, fall, winter and spring (figure 4.2). There are very little variations between the seasonal mean ADT patterns, especially with regards to the spatial structure of the AC system. The maximum ADT in summer and fall (e.g. 1.43m and 1.39m) reaches slightly higher values than the winter and spring seasons (e.g. 1.36m and 1.34m).

The variations between the four seasonal mean ADTs become more apparent when calculated as anomalies from the mean ADT (figure 4.3). For the summer and fall seasons there are mostly positive anomalies, with mean anomalies of $0.0103m$ and $0.0145m$, respectively. For the winter and spring seasons the anomalies are primarily negative, with mean anomalies of $0.0136m$ and $0.0135m$, respectively. The anomalies span between $\pm 0.13m$ and are primarily found in a zonal band from $35°S$ to $42°S$.

Vectors representing the mean surface geostrophic currents for the AC system calculated

from the seasonal summer mean ADT are shown to follow the contours of the seasonal mean ADT surface (figure 4.4, summer season) with expectedly stronger values where the ADT gradient is high. Velocity patterns for the other seasons (not shown) are very similar to the pattern shown for the summer season, as expected from the largely similar patterns in seasonal ADT. The velocities are strongest, reaching up to $1.4 ms^{-1}$, in the AC flowing southwestwards. High velocities in the ARC are also evident for the surface geostrophic flow, following the distinct meandering structure of the ARC. The surface currents are strongest in the southwest flowing AC and in the eastward flowing ARC. In the retroflection loop the flow is somewhat weaker as the position of the retroflection area is highly variable leading to a spatial smoother mean surface velocity field. South and east of Madagascar a current flowing towards the AC system is also evident, in agreement with the Southeast Madagascar Current.

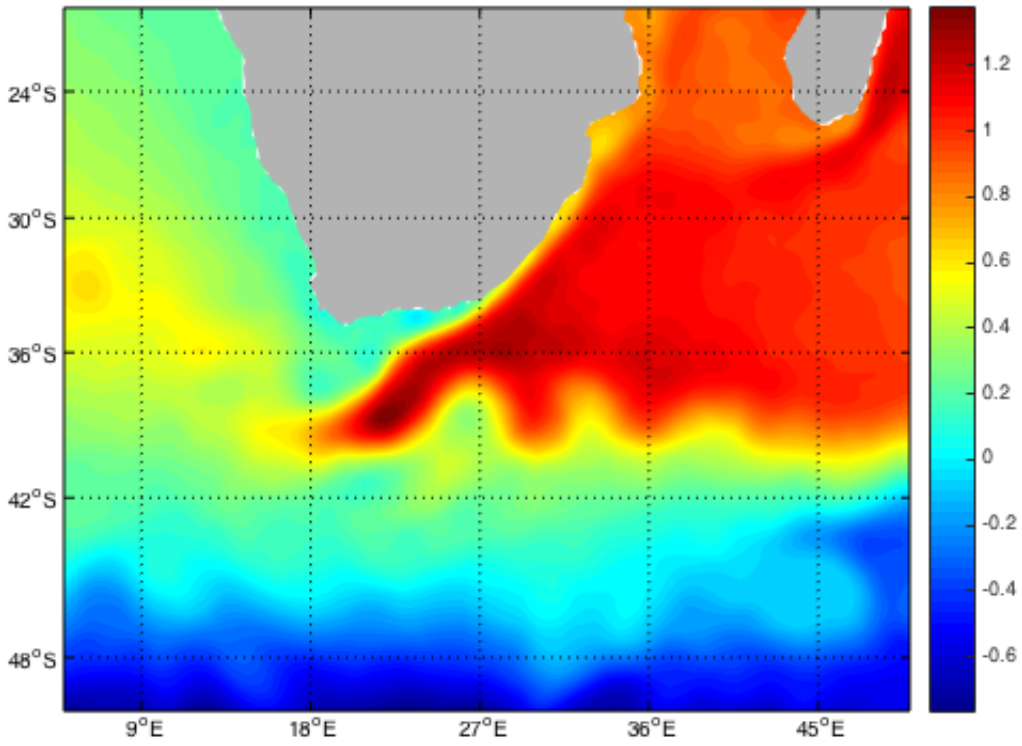

Figure 4.1: Mean absolute dynamic topography for the area around southern Africa averaged over the period 1993–2013. The ADT data are the delayed-time gridded altimetry product from Aviso and are given in meters relative to the geoid.

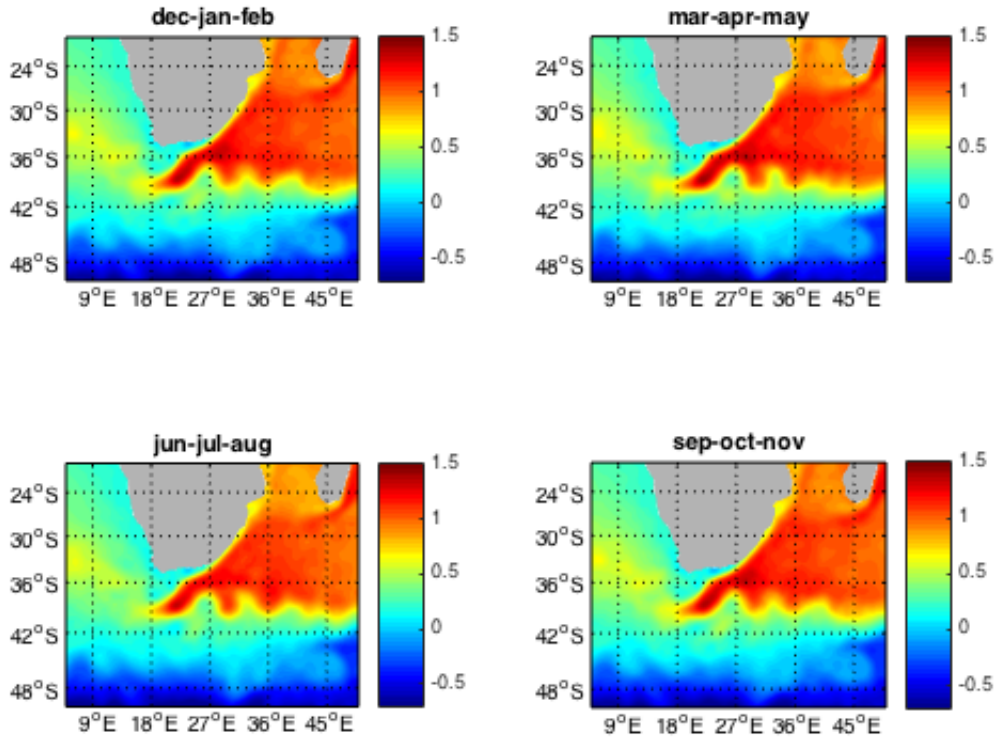

Figure 4.2: Seasonal averaged absolute dynamic topography for the area around southern Africa for the period 1993–2013. The ADT data are from the delayed-time gridded altimetry product from Aviso and are given in meters relative to the geoid. The seasonal mean is referred to the austral seasons: Dec-Jan-Feb is summer, Mar-Apr-May is fall, Jun-Jul-Aug is winter, Sep-Oct-Nov is spring.

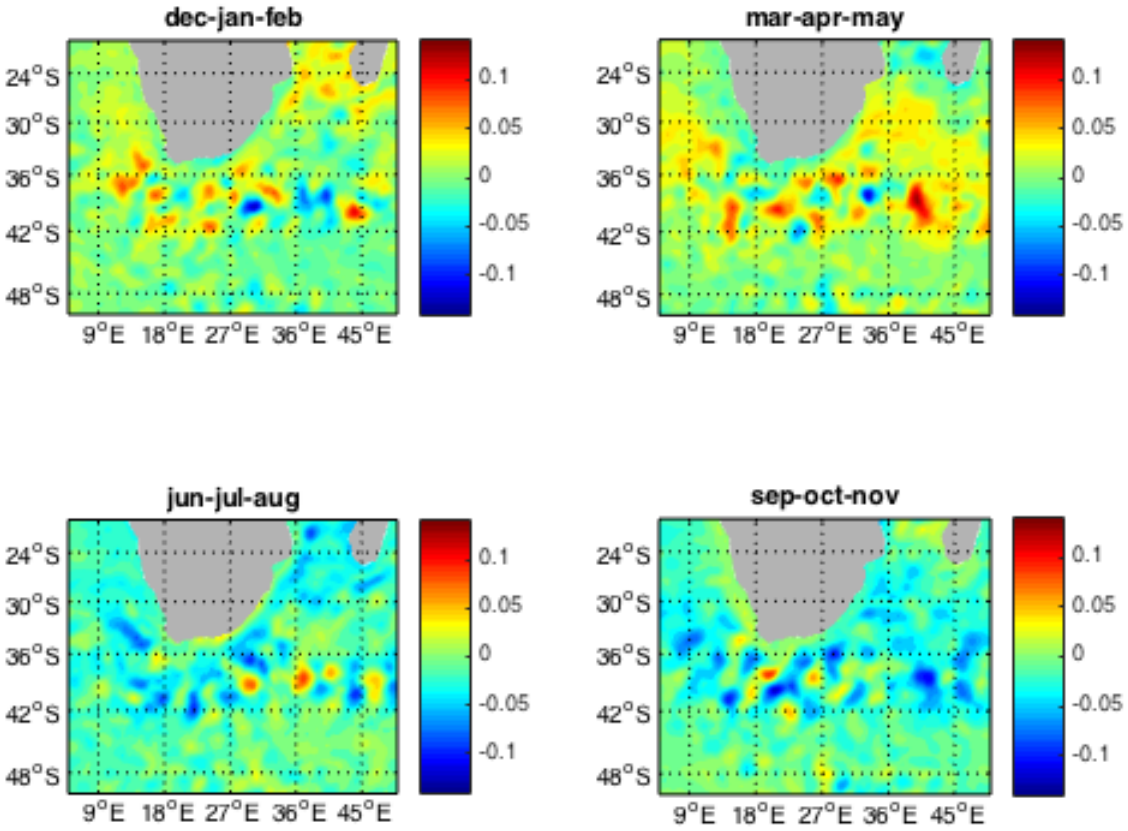

Figure 4.3: Seasonal anomalies of the absolute dynamic topography for the area around southern Africa averaged over the period 1993–2013. The ADT data are from the delayed-time gridded altimetry product from Aviso and are given in meters relative to the mean ADT (see figure 4.1). The seasonal anomalies are referred to the austral seasons: Dec-Jan-Feb is summer, Mar-Apr-May is fall, Jun-Jul-Aug is winter, Sep-Oct-Nov is spring.

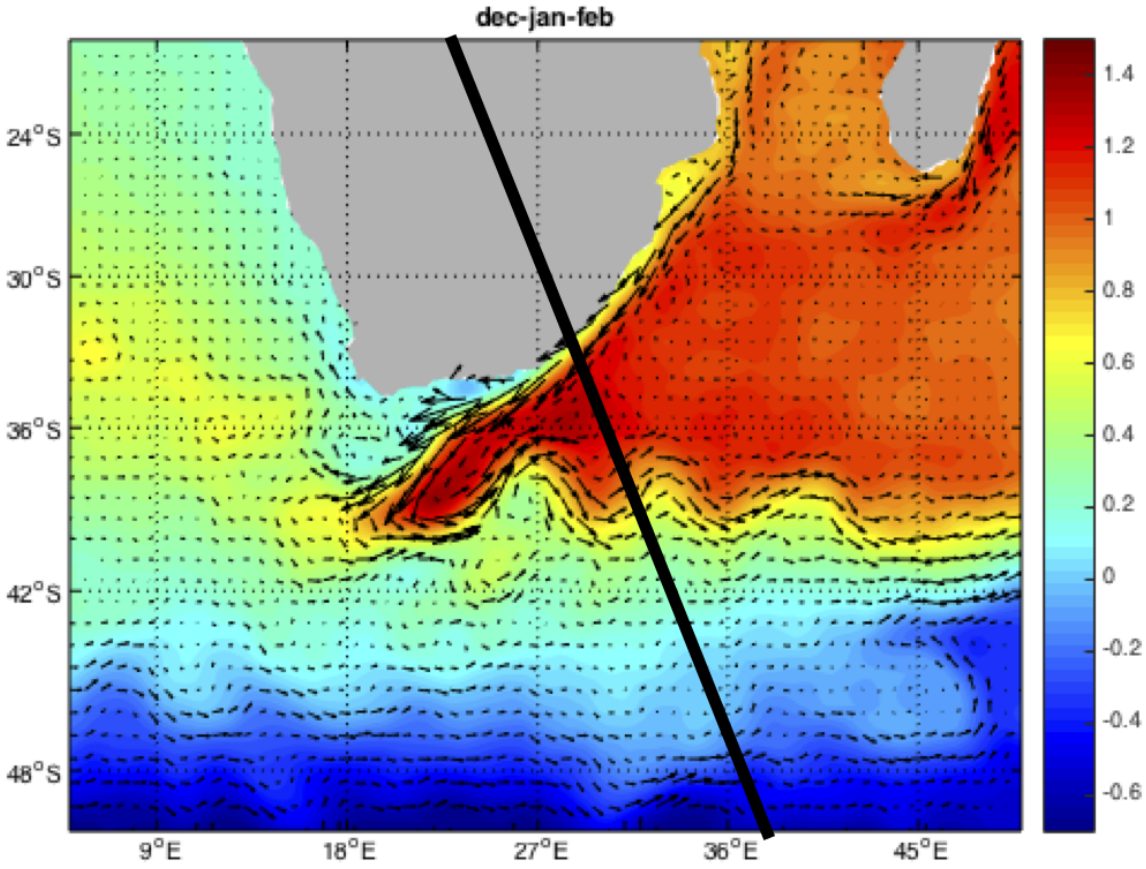

Figure 4.4: Mean austral summer (Dec-Jan-Feb) surface geostrophic velocities superimposed onto the absolute dynamic topography for the area around Southern Africa seasonally averaged over the period 1993–2013. The ADT data are from the delayed-time gridded altimetry product from Aviso and are given in meters relative to the geoid. Surface geostrophic velocities reach up to $1.3 ms^{-1}$ (vectors). The approximate ground track of track 96 is marked in black.

4.2 Along-track Variability

To investigate the variability on interannual time scales the repeat ground track 96 (black line in figure 4.4) covered by satellite altimeters since September 1992 is investigated. As noticed this track crosses both the AC and the ARC. The sea level anomalies (SLA) for the satellite track 96 over the period from September 1992 to May 2014 (figure 4.5) exhibit fluctuations reaching about $\pm 1m$ from the MDT. Largest anomalies are found between $38°S$ and $41°S$, but evidence of some strong negative anomalies and weaker positive anomalies are also depicted further north. The strongest positive anomalies in the band between $39°S$ and $41°S$ reach up to $1.1m$ above the MDT, whereas the strongest negative anomalies are found in a band slightly further north, between $38°S$ and $40°S$, with values down to $1m$ below the MDT. North of $34°S$ and south of $41°S$ the SLA are in comparison very small except from a few randomly distributed negative anomalies. In general, it is also noticed that there are more positive anomalies depicted in the period from 1999 to 2010.

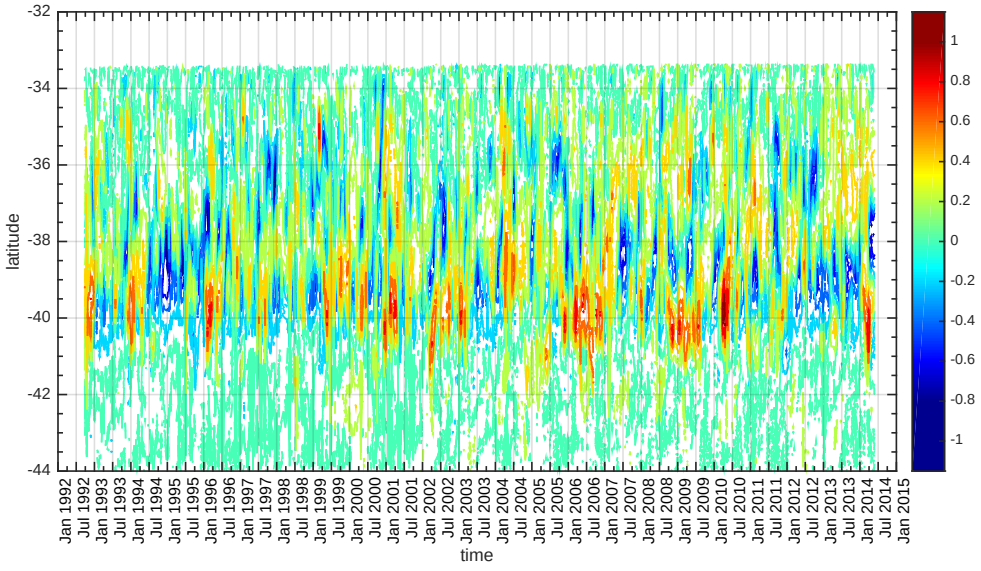

Figure 4.5: Hovmuller plot of the sea level anomalies for track 96, going southeast from Port Elizabeth, for the period September 1992–May 2014. The SLA data are from the delayed-time along-track altimetry data from Aviso and are given in meters from the mean dynamic topography. The repeat cycle for the satellites is 9.9156 days, giving data at approximately 10 days interval. White areas have no data.

The ADT for the satellite track 96 over the period from September 1992 to May 2014 (figure 4.6) highlights the steep and stable sea surface slope around 34°S as expected due to topographic steering of the AC in this region (de Ruijter et al., 1999). High values of ADT are found enclosed in the north by the AC and by the ARC meandering between 37°S and 40°S in the south. This temporal ADT pattern gives strong evidence of limited variability at the northern front of the AC as expected due to topographic steering. On the other hand the southern front of the ARC display larger meandering variability with north south migration up to three degrees latitude (333km). More high values of ADT are found from 2006-2014 than earlier in the time-series.

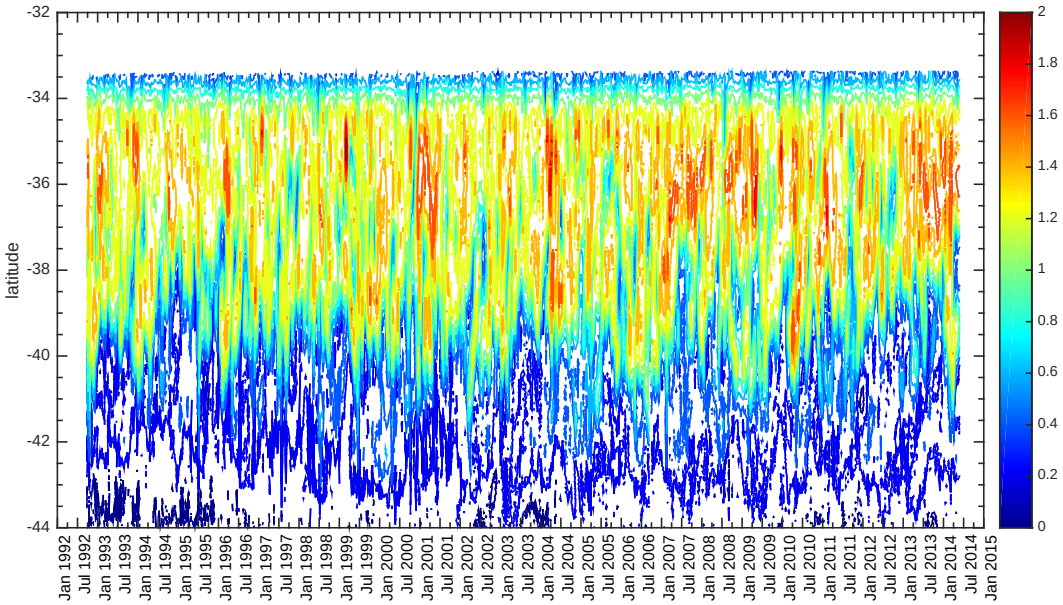

Figure 4.6: Absolute dynamic topography along track 96, going southeast from Port Elizabeth, for the period September 1992–May 2014. The ADT data are from the delayed-time along-track altimetry data from Aviso. The repeat cycle for the satellites is 9.9156 days, giving data at approximately 10 days interval. White areas have no data. The ADT is given in meters relative to the geoid.

The cross-track component of the sea surface geostrophic velocity (figure 4.7) is calculated from the along-track slope in the ADT. To enhance the mean signal, a limit of $\pm 0.1m$ is set for the difference in ADT between two consecutive data points. This leads to a surface geostrophic

velocity for the AC system reaching up to $2ms^{-1}$. The AC is seen north of $34°S$ where the mean velocity is $0.73ms^{-1}$ flowing in the southwestward direction. South of this the current is mostly giving an eastward flow. This easterly directed current component is often strongest between $38°S$ and $41°S$ revealing comparable meandering pattern of the southern termination of the ARC as seen in both the SLA and ADT plot.

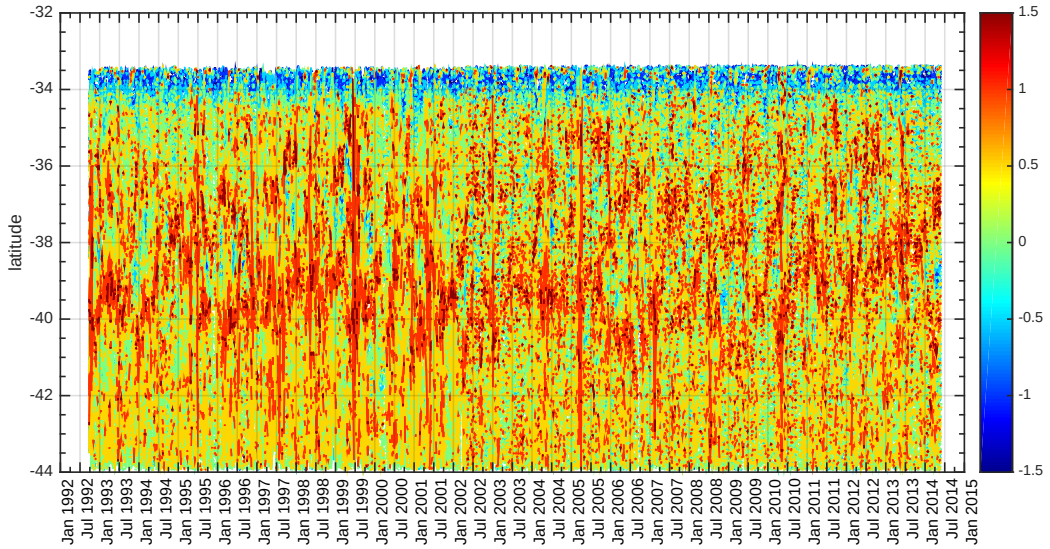

Figure 4.7: Surface geostrophic velocity along track 96, going southeast from Port Elizabeth, for the period September 1992–May 2014. The geostrophic velocities are calculated from the absolute dynamic topography. The ADT data are from the delayed-time along-track altimetry data from Aviso. The repeat cycle for the satellites is 9.9156 days, giving data at approximately 10 days interval. Velocities are given in ms^{-1}, cold/warm colors imply westerly/easterly directions.

The power spectra of the ADT at $39.5°S$ (figure 4.8) has two distinct peaks, the highest at 0.56 cycles per year and one at 0.23 cycles per year. These peaks represents cycles with periods of 1.8 and 4.3 years, respectively. The peak at 0.56 cycles per year is a multiple of several of the peaks at lower frequency ($0.047 \cdot 12$, $0.093 \cdot 6$, $0.140 \cdot 4$, $0.186 \cdot 3$, $0.280 \cdot 2$ - all of varying power), whereas the peak at 0.23 cycles per year is a multiple of the lowest frequency, $0.047 \cdot 5$. This can disturb the calculation of power per frequency. Then again, both peaks can be multiplied and coincide with higher frequency peaks, which is not evident, at least not in full strength.

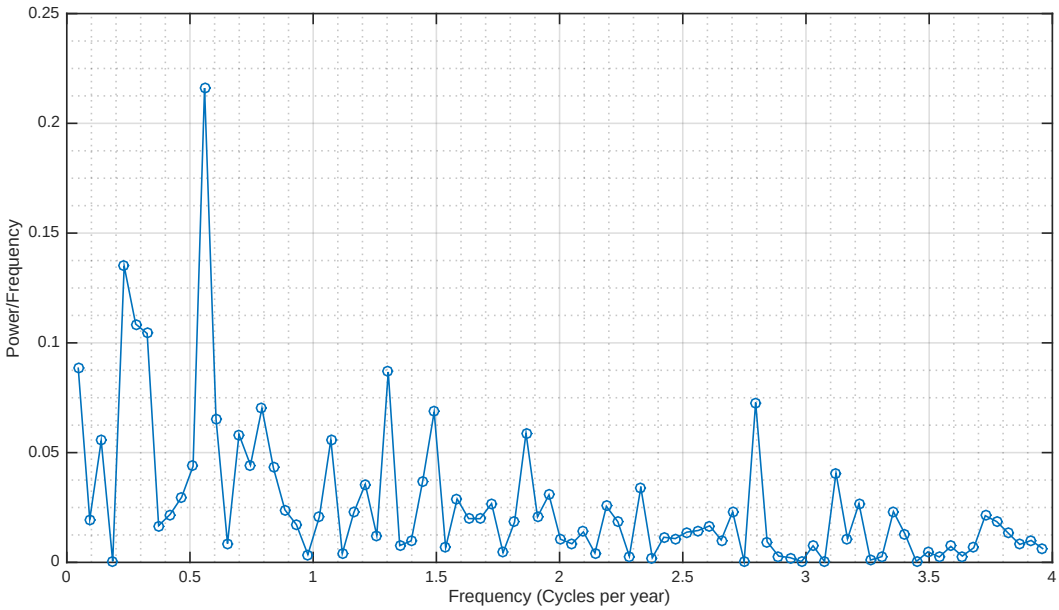

Figure 4.8: Spectral analysis of absolute dynamic topography at 39.5°S for the time series September 1992–May 2014. The figure is cut to show maximum frequency of 4 cycles per year, implying seasonal variations, down to minimum frequency of 0.05 cycles per year, yielding one cycle for the whole time series of 21.5 years.

4.3 Agulhas Retroflection Position

The ADT from the HYCOM free run is plotted as monthly means for the period 1980-2009. In an example from June 1980 (figure 4.9) black dots defining the area where SSH_{ref} is calculated and a black line tracing the contour of this value are shown. The monthly ADT pattern is similar to that of the mean ADT in figure 4.1 with the distinct structures associated with the topographic slopes defining the boundaries of the greater Agulhas Current system. The contour defined by the level surface SSH_{ref} can then be considered as an indicator of the pathway of the AC flow. The westernmost part of the contour defining the AC is marked by a blue dashed cross. The same plots are also made from gridded altimetry data for the years 1993-2013.

The SSH_{ref}-trajectories for all twelve months derived from the HYCOM simulation are averaged over 30 years (1980-2009) (figure 4.10). The same procedure is followed for 21 years (1993-2013) of gridded altimetry data (figure 4.11). For both datasets the trajectories are fairly stable along the southeast coast and shelf break of southern Africa. For the retroflection area, on the other hand, the HYCOM data are more variable and extending further west, between

$12°E-15°E$, than the gridded altimetry data, $19°E-20°E$. Moreover, for HYCOM field, the trajectories are almost zonal around $40°S-42°S$ in the return current area. For the gridded altimetry data, on the other hand, the trajectories meanders horizontally between $37°S$ and $40°S$.

The westernmost position of the AC defined by the blue dashed cross in figure 4.9 is shown for 30 years of the monthly values from the HYCOM simulation (blue dots in figure 4.12) and for 21 years of the monthly gridded altimeter-based ADT data (red dots in figure 4.12). The different length of the time series, give a difference of more than hundred data points. As noticed, the HYCOM data have a much larger spread, mainly between $5°E$ and $23°E$, than the gridded altimetry data that are concentrated mainly between $15°E$ and $22°E$. This is a difference in spread of more than ten degrees longitude. At $40°S$, a distance of one degree in longitude is about $85km$. This

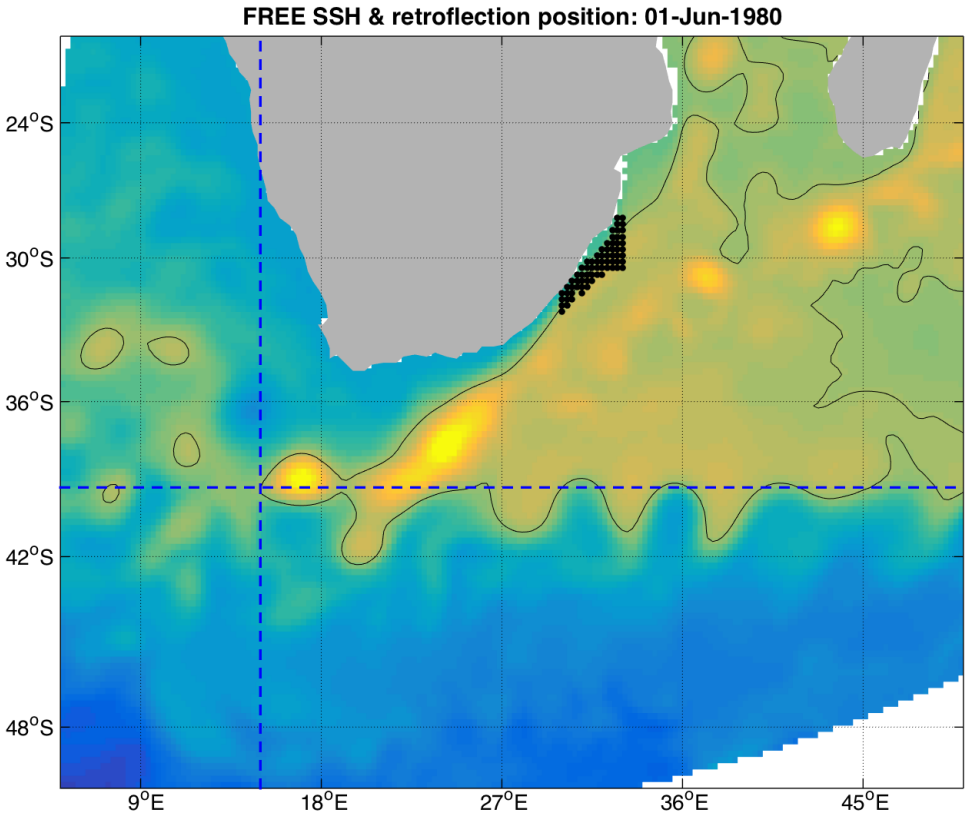

Figure 4.9: The absolute dynamic topography for the area around southern Africa for 01 June 1980 derived from HYCOM. The black dots are the data points used to calculate SSH_{ref}, and the black contour is the trajectory representing this reference value. The blue dashed cross points out the westernmost position of the retroflection.

entails that the spread in retroflection position for the HYCOM data is more than 1500km, and for the gridded altimetry data the spread is about 600km. The Good Hope line is marked in black, and marks the position used for measuring the magnitude of Agulhas leakage (van Sebille et al., 2009). The HYCOM data display many occurrences where the AR is positioned beyond this line. In contrast, the AR position is never on the Atlantic westward side of this line for the gridded altimetry data.

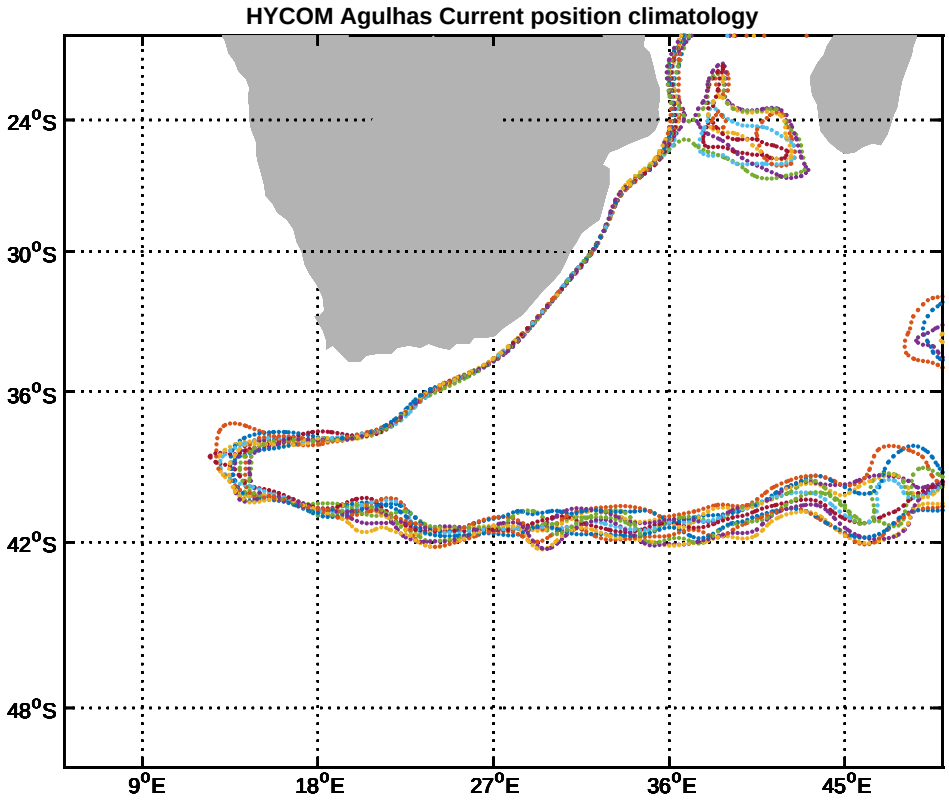

Figure 4.10: Contours defined by SSH_{ref} representing the pathway of the greater Agulhas Current system. The reference values are monthly averaged from the HYCOM simulation over the years 1980-2009.

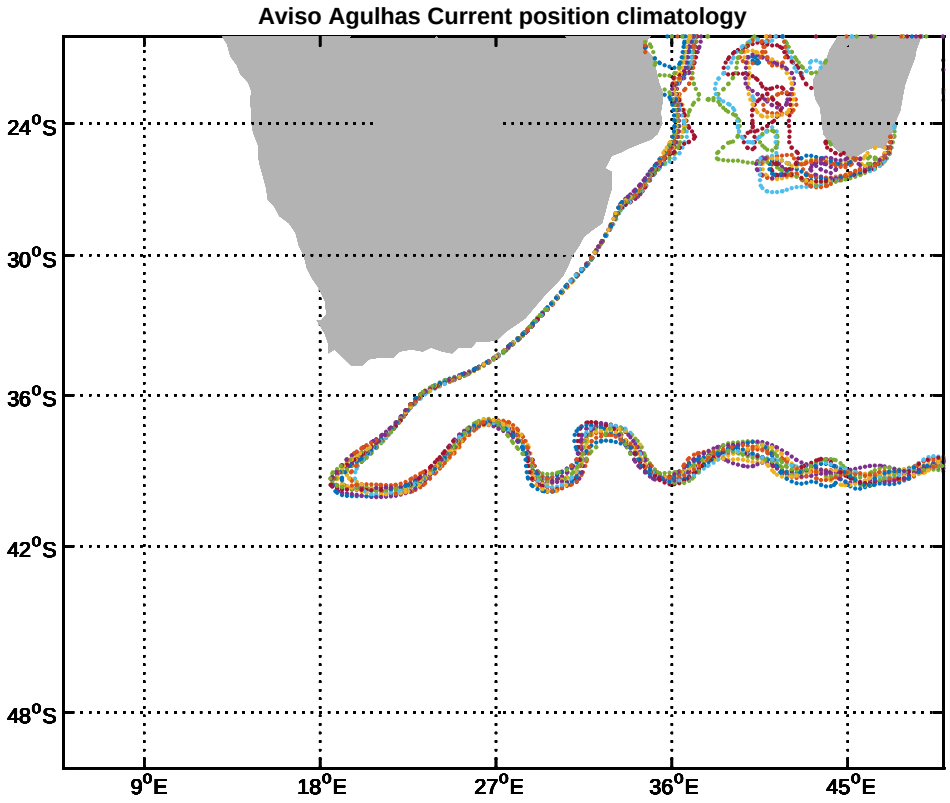

Figure 4.11: Contours defined by SSH_{ref} representing the pathway of the greater Agulhas Current system. The reference values are monthly averaged over the years 1993-2013. The ADT data are from the delayed-time gridded altimetry product from Aviso.

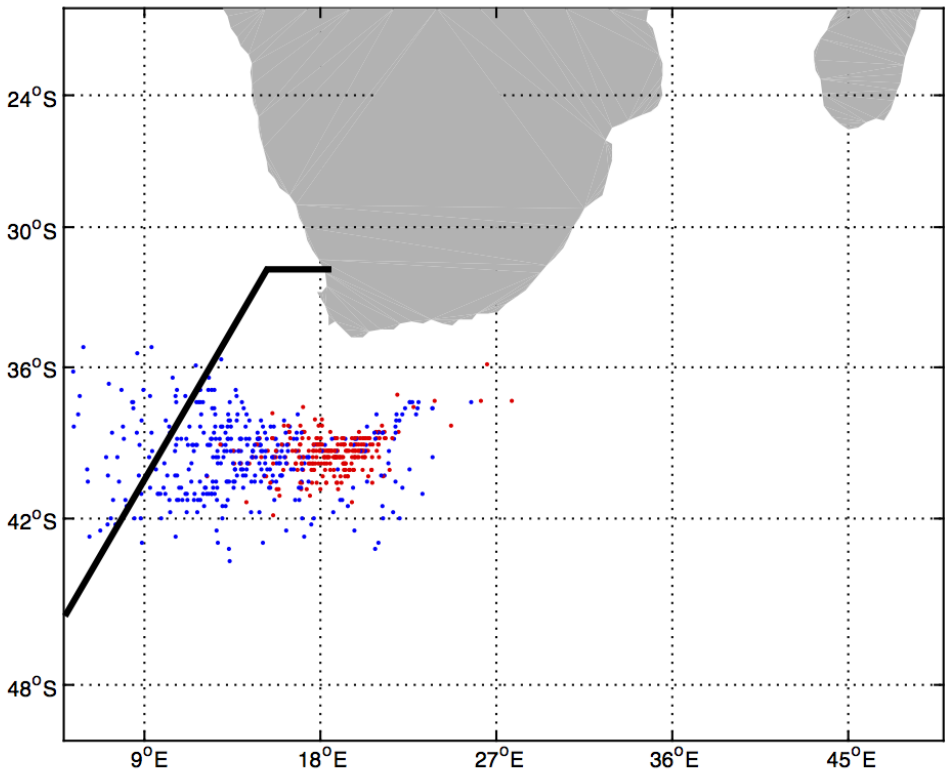

Figure 4.12: The monthly positions of the Agulhas Retroflection as defined by the westernmost location of the SSH_{ref} for the HYCOM data (blue dots, 1980-2009), and for the gridded altimetry data (red dots, 1993-2013). The black line is the approximate position of the Good Hope line.

Chapter 5

Discussion

5.1 Seasonality

The topographic steering of the Agulhas Current (AC) gives a very stable flow pattern (de Ruijter et al., 1999). In the AC system the spatial patterns of the seasonal mean ADT (figure 4.2) are almost identically to each other and to the mean climatology (figure 4.1). The small variations exhibited by the anomalies in the ADT (figure 4.3) only varies around $\pm 0.2m$ and might be due to the thermo-steric effect as the warm seasons, summer and fall, have the most positive ADT anomalies. However, Krug and Tournadre (2012) found similar seasonal variations from altimetry data for the AC area and tested this against seasonal sea surface temperature with the conclusion that the seasonality was not induced by the steric effect.

The surface geostrophic current is directly linked to the ADT pattern (Robinson, 2004), and has the same weak positive anomaly in summer (figure 4.4) and fall. The weaker gradient in the ADT, and consequently the weaker surface geostrophic current velocities, in the Agulhas Retroflection (AR) area indicate distinct variability in the AR position. The seemingly stability of the Agulhas Return Current (ARC) is partly due to the Agulhas Plateau (Boebel et al., 2003) that steers the current northwards around $25°E$ and generates the lateral meanders downstream.

The large features of the AC system varies little with season, both in strength and spatial structure and are in agreement with most observational studies on the seasonality of the AC (e.g. Bryden et al. (2005), Matano et al. (2008)). As the seasonal variations are small, the analysis will now focus on variability on the longer timescales.

5.2 Inter-annual Variability

North of 34°S the lack of SLA (figure 4.5) highlights the temporal stability of the AC. Only a few negative anomalies are found here, and are most likely explained by offshore displacement of the AC associated with southward propagation of meanders at the inshore border of the AC (Rouault and Penven, 2011), known as Natal Pulses. The steep and stable gradient in the ADT north of 34°S (figure 4.6) confirms the stability of the AC. A few low values of ADT are also present in this plot, with reference to equation 2.14, obviously corresponding to the negative SLA in this area.

The inter-annual north-south fluctuations of the ARC between 38°S and 41°S agrees well with the quasi-stationary meandering pattern for the period 1997-1999 (38°S to 40°S) presented by Boebel et al. (2003). They found that the peak surface velocities decrease from 2.1ms^{-1} near the AR to 1.1ms^{-1} around 32°E. Ground track 96 from along-track altimetry data crosses the ARC around 32°E and velocities (figure 4.7) are found to be around 1ms^{-1} and occasionally up to 1.5ms^{-1}. There is a clear variability in the north-south fluctuation of ARC along track 96, and a representative time series of the ADT at 39.5°S is extracted for determination of inter-annual frequencies through a spectral analysis.

The main peaks in the power spectrum (figure 4.8) are found at the frequencies of 0.56 and 0.23 cycles per year, corresponding to cycles with periods of 1.8 and 4.3 years, respectively. No known phenomena match these frequencies, and few or no studies have been made on the temporal variation of the ARC. The fact that these frequencies are multiples of lower frequencies, especially the 0.56 cycles per year frequency, might contaminate the results. However, these lower frequencies vary in strength and the influence on the power spectra signal is uncertain. Also higher frequencies are multiples of 0.56 and 0.23 cycles per year, but do not show with high power in the spectral analysis. For the sake of clarity, the frequency corresponding to an annual cycle (1 cycle per year), has a spectral peak close to zero.

5.3 Inter-basin Indian-Atlantic Ocean Exchange

For the 21 years of gridded altimetry data and the 30 years of HYCOM data the monthly position of the AR is tracked allowing for investigation of the east-west position of the retroflec-

tion. According to van Sebille et al. (2009) smaller/larger AC transport leads to larger/smaller Indian-Atlantic exchange. As such a stronger current will therefore expectedly be associated with an early retroflection and larger return flow. In contrast, a weak current will maintain a later retroflection which leads to more ring shedding and inter-ocean exchange. Both the length of the time series and the spatial resolution differs between the two datasets, and can partly explain why HYCOM exhibit more variability compared to the gridded altimetry data. The simulation length for HYCOM of 30 years gives more variability than the 21 years of gridded altimetry data. The spatial resolution of HYCOM resolves phenomenon of length scale down to 30 km. In comparison, the gridded altimetry data only resolves phenomenon of length scale down to 50-75 km. The better resolution of HYCOM generates more variability.

By comparing HYCOM (figure 4.10) and gridded altimetry (figure 4.11) maps of the AC system, it seems that HYCOM has some difficulties when it comes to the position of the AR and the subsequent location of the ARC. The AR position is often too far west (figure 4.12), and the meandering ARC is too far south and not meandering. (Backeberg et al., 2008) stated that the position of the retroflection in HYCOM is fairly well represented in the longer term mean. In a resent study by Backeberg et al. (2015) the position of the AR from HYCOM data is investigated. Many factors governing the model simulation of the retroflection position were detected, and in particular a more realistic representation of the deep currents, improves the simulation of the position of the AR.

van Sebille et al. (2010) stated that the Good Hope line (marked in figure 4.12) is a suitable section for measuring the magnitude of Agulhas leakage. The retroflection position does not have to be on the far side of this line to contribute to the Agulhas leakage. Half the modeled floats passing 19°E, representing the mean AR position, passed the Good Hope line. The gridded altimetry data give a mean position of the AR at 19°E, the HYCOM data give a mean position of the AR at 14°E and are expected to simulate more leakage. The magnitude of the leakage is estimated to be $10-20\%$ of the AC inflow transport (de Ruijter et al. (1999), van Sebille et al. (2009)), the rest is retroflected and flows eastwards in a meandering pattern that forms the ARC. Further east, the water in the ARC is recirculated into the West-Indian sub-gyre (Lutjeharms, 2006a).

Current speed is not necessarily a good estimation for volume transport, but can be used as

an indicator. For the gridded altimetry data the velocity of the surface geostrophic current of the AC are calculated to reach up to $1.4 ms^{-1}$. Backeberg et al. (2008) compared surface geostrophic velocity fields from the gridded altimetry data and the HYCOM data. The surface geostrophic velocity field from HYCOM was found to be more intense. Hence, the larger inter-ocean exchange and larger variability in the position of the AR can not be explained by the results of van Sebille et al. (2009).

As the dominating dynamics in the AR are highly non-linear and complex it is very challenging to define an indicator for the eddy shedding based on satellite data. This is clearly confirmed in the analysis of the ADT and the surface geostrophic current data, and is further documented from corresponding analyses of the satellite based sea surface temperature data (J. A. Johannesen, personal communication).

Chapter 6

Conclusion

6.1 Summary and Conclusions

The spatial pattern in the ADT provides a distinct and robust structure of the greater Agulhas Current regime and reveals minor temporal variability except in the ARC. Moreover, the seasonal ADT anomalies are slightly higher and the seasonal geostrophic velocities are slightly stronger in the austral summer and fall compared to the winter and spring seasons.

In the ARC the along-track altimetry data (track 96) show clear inter-annual variability. Spectral analysis indicates that the dominating variability have periods of 1.8 and 4.3 years. In comparison, no interannual variability are detected for the AC, except for the occasional negative anomalies indicating the passages of Natal Pulses.

The AC simulated by HYCOM corresponds well to that observed by the gridded altimetry data. The mean position of the ARC, however, is about two degrees too far south and lack the characteristic meanders that are well displayed by the gridded altimetry data. Moreover, also the mean position of the AR simulated by HYCOM differs from that observed by the altimetry data. The longer time series and higher resolution of the HYCOM data can partly explain why the model exhibits more variability than the gridded altimetry data.

The position of the AR represented by HYCOM data varies more than 18 degrees in east-west direction, with its westernmost position at $5^{\circ}E$. In contrast, the gridded altimetry data depict an east-west variations of the AR position of about seven degrees, with its westernmost position at $14^{\circ}E$. In comparison, the observed and simulated fields provided no distinct evidence for a

reliable indicator of the retroflection position. This is most likely due to the high non-linear and complex dynamics that are present in this region.

6.2 Recommendations for Further Work

The findings and achievements reported in this study could benefit from a further assessment and inter-comparison using in-situ data such as surface drifters and profiling Argo floats. In particular, the dynamics in the retroflection region and its relation with the eddy shedding and transport of warm saline water into the South Atlantic need further careful investigation. Improved knowledge of this would, in turn, shed more light on the variability of volume and heat transport in the ARC.

Radar altimeter observations from at least two missions is sustained for the next 10-15 years. This means that the altimeter-based study of mesoscale dynamic variability can be continued and combined with the growing amount of in-situ data from autonomous floats and moorings. As such the length of the data record will also gradually allow for seasonal to decadal variability studies.

Moreover, through data assimilation in HYCOM more realistic simulations of the greater Agulhas Current regime can be carried out. Improved understanding of the dynamics will then be obtained that, in turn, can strengthen the design, implementation and maintenance of the observing system.

Appendix A

Acronyms

AC Agulhas Current

ADT Absolute Dynamic Topography

AMOC Atlantic Meridional Overturning Circulation

ARC Agulhas Return Current

AR Agulhas Retroflection

AVISO Archiving, Validating and Interpretation of Satellite Oceanographic Data

CNES Centre National d'Etudes Spatiales (French Space Agency)

DUACS Developing Use of Altimetry for Climate Studies/Data Unification and Altimeter Combination System

EMC East Madagascar Current

ERS-1 European Remote-Sensing Satellite 1

ERS-2 European Remote-Sensing Satellite 2

ESA European Space Agency

FFT Fast Fourier Transform

GOCE Gravity field and steady-state Ocean Circulation Explorer

GRACE Gravity Recovery and Climate Experiment

HYCOM HYbrid Coordinate Ocean Model

J-1 Jason-1

J-2 Jason-2

MC Mozambique Channel

MDT Mean Dynamic Topography

MSS Mean Sea Surface

NASA National Aeronautics and Space Administration

NERSC Nansen Environmental and Remote Sensing Center

NTC Nansen-Tutu Center

SCAMPI the Seasonal to decadal Changes Affecting Marine Productivity: an Interdisciplinary investigation

SLA Sea Level Anomalies

SSH Sea Surface Height

SSH$_{ref}$ Reference value of Sea Surface Height

SSALTO Segment Sol multi-missions dALTimetrie, d'orbitographie et de localisation precise

T/P TOPEX/Poseidon

UCT University of Cape Town

Bibliography

Backeberg, B. C., Counillon, F., Johannessen, J. A., and Pujol, M.-I. (2014). Assimilating along-track SLA data using the EnOI in an eddy resolving model of the Agulhas system. *Ocean Dynamics*, 64(8):1121–1136.

Backeberg, B. C., Deshayes, J., Bezaud, M., Johannessen, J. A., and Reason, C. J. C. (2015). Modelling Agulhas Current System dynamics: the butterfly effect of changing the vertical stratification. *Ocean Modelling, in review*.

Backeberg, B. C., Johannessen, J. A., Bertino, L., and Reason, C. J. C. (2008). The greater Agulhas Current system: An integrated study of its mesoscale variability. *Journal of Operational Oceanography*, 1(1):29–44.

Backeberg, B. C., Penven, P., and Rouault, M. (2012). Impact of intensified Indian Ocean winds on mesoscale variability in the Agulhas system. *Nature Climate Change*, 2(8):608–612.

Beckley, B. D., Zelensky, N. P., Holmes, S. A., Lemoine, F. G., Ray, R. D., Mitchum, G. T., Desai, S. D., and Brown, S. T. (2010). Assessment of the Jason-2 extension to the TOPEX/Poseidon, Jason-1 sea-surface height time series for global mean sea level monitoring. *Marine Geodesy*, 33(S1):447–471.

Biastoch, A., Böning, C. W., Schwarzkopf, F. U., and Lutjeharms, J. (2009). Increase in Agulhas leakage due to poleward shift of Southern Hemisphere westerlies. *Nature*, 462(7272):495–498.

Biastoch, A., Reason, C. J. C., Lutjeharms, J. R. E., and Boebel, O. (1999). The importance of flow in the Mozambique Channel to seasonality in the greater Agulhas Current system. *Geophysical research letters*, 26(21):3321–3324.

Bleck, R. (2002). An Oceanic general circulation model framed in hybrid isopycnic-Cartesian coordinates. *Ocean Modelling*, 4(1):55–88.

Boebel, O., Rossby, T., Lutjeharms, J., Zenk, W., and Barron, C. (2003). Path and variability of the Agulhas Return Current. *Deep Sea Research Part II: Topical Studies in Oceanography*, 50(1):35–56.

Bosch, W., Dettmering, D., and Schwatke, C. (2014). Multi-Mission Cross-Calibration of Satellite Altimeters: Constructing a Long-Term Data Record for Global and Regional Sea Level Change Studies. *Remote Sensing*, 6(3):2255–2281.

Bryden, H., Beal, L., and Duncan, L. (2005). Structure and Transport of the Agulhas Current and Its Temporal Variability. *Journal of Oceanography*, 61(3):479–492.

Capet, A., Mason, E., Rossi, V., Troupin, C., Faugère, Y., Pujol, I., and Pascual, A. (2014). Implications of refined altimetry on estimates of mesoscale activity and eddy-driven offshore transport in the Eastern Boundary Upwelling Systems. *Geophysical Research Letters*, 41(21):7602–7610.

de Ruijter, W. P., van Leeuwen, P. J., and Lutjeharms, J. R. (1999). Generation and evolution of Natal Pulses: solitary meanders in the Agulhas Current. *Journal of physical oceanography*, 29(12):3043–3055.

Duacs/AVISO (2014). *A new version of SSALTO/Duacs products available in April 2014*. CNES, http://www.aviso.altimetry.fr/fileadmin/documents/data/duacs/Duacs2014.pdf, version 1.1 edition.

Gill, A. E. (1982). *Atmosphere-ocean dynamics*, volume 30. Academic press.

Hermes, J. C., Reason, C. J. C., and Lutjeharms, J. R. E. (2007). Modeling the Variability of the Greater Agulhas Current System. *Journal of Climate*, 20(13):3131–3146.

Johannessen, J. A., Balmino, G., Le Provost, C., Rummel, R., Sabadini, R., Sünkel, H., Tscherning, C., Visser, P., Woodworth, P., and Hughes, C. (2003). The European gravity field and steady-state ocean circulation explorer satellite mission its impact on geophysics. *Surveys in Geophysics*, 24(4):339–386.

Johannessen, J. A., Raj, R. P., Nilsen, J. E. Ø., Pripp, T., Knudsen, P., Counillon, F., Stammer, D., Bertino, L., Andersen, O. B., Serra, N., and Koldunov, N. (2014). Toward Improved Estimation of the Dynamic Topography and Ocean Circulation in the High Latitude and Arctic Ocean: The Importance of GOCE. *Surveys in Geophysics*, 35(3):661–679.

Krug, M. and Tournadre, J. (2012). Satellite observations of an annual cycle in the Agulhas Current. *Geophysical Research Letters*, 39(15).

Lutjeharms, J. R. E. (2006a). *The Agulhas Current*. Springer.

Lutjeharms, J. R. E. (2006b). The coastal oceans of south-eastern Africa (15, W). *The sea*, 14:783–834.

Matano, R., Beier, E., and Strub, P. (2008). The seasonal variability of the circulation in the South Indian Ocean: Model and observations. *Journal of Marine Systems*, 74(1–2):315 – 328.

Matano, R. P., Beier, E. J., Strub, P. T., and Tokmakian, R. (2002). Large-Scale Forcing of the Agulhas Variability: The Seasonal Cycle. *Journal of Physical Oceanography*, 32(4):1228–1241.

Matano, R. P., Simionato, C. G., de Ruijter, W. P., van Leeuween, P. J., Strub, P. T., Chelton, D. B., and Schlax, M. G. (1998). Seasonal variability in the Agulhas Retroflection Region. *Geophysical Research Letters*, 25(23):4361–4364.

Matano, R. P., Simionato, C. G., and Strub, P. T. (1999). Modeling the Wind-Driven Variability of the South Indian Ocean. *Journal of Physical Oceanography*, 29(2):217–230.

Mazloff, M. R., Gille, S. T., and Cornuelle, B. (2014). Improving the geoid: Combining altimetry and mean dynamic topography in the California coastal ocean. *Geophysical Research Letters*, 41(24):8944–8952.

Nerem, R. S., Chambers, D. P., Choe, C., and Mitchum, G. T. (2010). Estimating Mean Sea Level Change from the TOPEX and Jason Altimeter Missions. *Marine Geodesy*, 33(sup1):435–446.

Rio, M., Mulet, S., and Picot, N. (2014). Beyond GOCE for the ocean circulation estimate: Synergetic use of altimetry, gravimetry, and in situ data provides new insight into geostrophic and Ekman currents. *Geophysical Research Letters*.

Rizos, C., Willis, P., Pail, R., Albertella, A., Rieser, D., Brockmann, J., Schuh, W.-D., and Savcenko, R. (2014). *International Association of Geodesy Symposia*, volume 139, pages 275–281. Springer Berlin Heidelberg.

Robinson, I. S. (2004). *Measuring the oceans from space: the principles and methods of satellite oceanography*. Springer Science & Business Media.

Rouault, M. J. and Penven, P. (2011). New perspectives on Natal Pulses from satellite observations. *Journal of Geophysical Research: Oceans (1978–2012)*, 116(C7).

SCAMPI (2014). Project description: SCAMPI.

Talone, M., Meloni, M., Pelegri, J. L., Rosell-Fieschi, M., and Flobergaghen, R. (2014). Evolution of geoids in recent years and its impact on oceanography. *Scientia Marina*, 78(2):155–164.

Traon, P. Y. and Dibarboure, G. (2004). An Illustration of the Contribution of the TOPEX/Poseidon–Jason-1 Tandem Mission to Mesoscale Variability Studies. *Marine Geodesy*, 27(1-2):3–13.

van Sebille, E., Beal, L. M., and Biastoch, A. (2010). Sea surface slope as a proxy for Agulhas Current strength. *Geophysical Research Letters*, 37(9).

van Sebille, E., Biastoch, A., van Leeuwen, P. J., and de Ruijter, W. P. M. (2009). A weaker Agulhas Current leads to more Agulhas leakage. *Geophysical Research Letters*, 36(3).